Petrogenesis of Volcanogenic Sedimentary Lithium Ore in the Neogene Macusani Volcanic Field, Puno, Peru

Johan Ramirez-Briones, Lisard Torró, Massimo Chiaradia, Oscar Laurent, Stéphanie Mandrou, Lorenzo Tavazzani, Cyril Chelle-Michou, Jean Vallance, Patrice Baby

▶ To cite this version:

Johan Ramirez-Briones, Lisard Torró, Massimo Chiaradia, Oscar Laurent, Stéphanie Mandrou, et al.. Petrogenesis of Volcanogenic Sedimentary Lithium Ore in the Neogene Macusani Volcanic Field, Puno, Peru. Journal of Petrology, 2025, 66 (5), pp.egaf041. ⟨10.1093/petrology/egaf041⟩. ⟨hal-05391088⟩

HAL Id: hal-05391088
https://hal.science/hal-05391088v1

Submitted on 2 Dec 2025

OXFORD UNIVERSITY PRESS | Journal of Petrology

Petrogenesis of Volcanogenic Sedimentary Lithium Ore in the Neogene Macusani Volcanic Field, Puno, Peru

Journal:	*Journal of Petrology*
Manuscript ID	JPET-Oct-24-0197.R1
Manuscript Type:	Original Manuscript
Date Submitted by the Author:	02-Mar-2025
Complete List of Authors:	RAMIREZ-BRIONES, JOHAN; Pontifical Catholic University of Peru TORRÓ, Lisard; Pontifical Catholic University of Peru Chiaradia, Massimo; University of Geneva, Department of Mineralogy Laurent, Oscar; Geosciences Environnement Toulouse MANDROU, STÉPHANIE; Laboratoire Geosciences Environnement Toulouse Tavazzani, Lorenzo; ETH Zurich, Erdwissenschaften Chelle-Michou, Cyril; ETH Zurich, Erdwissenschaften VALLANCE, JEAN; Pontifical Catholic University of Peru BABY, PATRICE; Pontifical Catholic University of Peru; Geoscience Environment Toulouse
Keyword:	macusanite, Neogene Ignimbrite Province of the Central Andes, peraluminous, rare metal granites, volcanogenic lithium deposits
Journal of Petrology now offers Virtual Collections of published papers. You may choose up to three collections from the list below. Virtual collections will increase the visibility of your work.:	Ore Deposits Formation < Process Themes

Petrogenesis of Volcanogenic Sedimentary Lithium Ore in the Neogene Macusani Volcanic Field, Puno, Peru

JOHAN S. RAMIREZ-BRIONES[1], LISARD TORRÓ[1,*], MASSIMO CHIARADIA[2], OSCAR LAURENT[3], STÉPHANIE MANDROU[3], LORENZO TAVAZZANI[4], CYRIL CHELLE-MICHOU[4], JEAN VALLANCE[1] and PATRICE BABY[1,3]

[1] *Geological Engineering Program, Faculty of Sciences and Engineering, Pontifical Catholic University of Peru (PUCP), Av. Universitaria 1801, San Miguel, Lima 15088, Peru*

[2] *Department of Earth Science, University of Geneva, Rue des Maraîchers, 13, 1205, Geneva, Switzerland*

[3] *Géosciences Environnement Toulouse, Université de Toulouse, CNES, CNRS, IRD, UPS, Av. Edouard Belin 14, Toulouse 31400, France*

[4] *Institute of Geochemistry and Petrology, ETH Zürich, Clausiusstrasse 25, Zürich CH-8092, Switzerland*

Submitted to *Journal of Petrology*

Running title: Petrogenesis of Volcanogenic Lithium Ore in Macusani

*Corresponding author: Lisard Torró, lisardtorro@hotmail.com

Phone: (+51) 6262000 Ext. 5060

ABSTRACT

The recently discovered Falchani volcanogenic sedimentary lithium deposit, situated within the Neogene Macusani Volcanic Field in SE Peru, represents one of the world's most significant resources of this metal. The Li ore is mainly hosted in the so-called Lithium-rich Tuff, a tuffaceous mudstone that is sandwiched between two Li-rich volcaniclastic units (Upper and Lower Breccia). The major and trace element composition of the Li-ore units differs from that of previously reported ash-flow tuff in the Macusani Volcanic Field. Rather, it approximates the chemistry of highly evolved peraluminous obsidian glasses, known as macusanite, and exhibits the characteristic geochemical fingerprint of peraluminous rare-metal granites and Li-Cs-Ta (LCT) pegmatites. The parental magmas of the Li-ore units have been modeled as containing <25 % of a mantle component with the isotopic signature of potassic to ultra-potassic basaltic melts. The remaining is attributed to partial melts of Proterozoic and Paleozoic paragneiss and metapelites. High fluorine activity in the melt lowered the solidus and delayed fluid-melt immiscibility, promoting high degrees of differentiation through fractional crystallization. Pre-eruptive metasomatic processes in the upper part of the crystal mush could have increased the concentration of Li and other fluid-mobile elements. Contrary to many volcanogenic sedimentary lithium deposits worldwide, in situ post-depositional metasomatic processes associated with the formation of secondary clay and zeolite assemblages did not result in lithium enrichment, but in its partial leaching. Falchani represents a first documentation of a volcanogenic sedimentary deposit where the primary lithium enrichment to economic grades was related to pre-eruptive magmatic processes.

Keywords: Central Andes; macusanite; peraluminous; rare metal granites; volcanogenic sedimentary lithium deposits

INTRODUCTION

The Neogene magmatic history of the Central Andes is marked by large-scale caldera- and ignimbrite-forming eruptive events (de Silva, 1989a, b; de Silva & Gosnold, 2007; Ward et al., 2017; de Silva & Kay, 2018). These events have led to the formation of one of the largest ignimbrite provinces on Earth, the so-called Neogene Ignimbrite Province of the Central Andes, which extends from southern Peru to western Argentina (Baker, 1981; de Silva et al., 2006; Fig. 1). It includes regionally extensive dacitic to rhyolitic monotonous ignimbrite sheets, cake-shaped domes, and large multi-phase calderas and ignimbrite-dome complexes (Baker, 1981; Gardeweg & Ramirez, 1987; Lindsay et al., 2001; de Silva et al., 2006). Several ignimbrite eruptions have occurred since the end of the Oligocene (e.g., Noble et al., 1974; Cheilletz et al., 1992; Wörner et al., 2000; Salisbury et al., 2011).

Changes in plate-tectonic conditions, including subduction geometry and thickness and thermal regimes of the Andean crust, and the existence of different lithospheric domains have impacted the distribution and composition of magmas along the Neogene Ignimbrite Province of the Central Andes (Wörner et al., 2018). Most of the ignimbritic activity has concentrated along successive arcs (main-arc domain), including the active Central Volcanic Zone (e.g., Siebel et al., 2001), stretching along the Western Cordillera and western boundary of the Altiplano plateau (Ramos, 2018). Peripheral, continent-ward to the main arc, a series of discrete, isolated ignimbrite fields occur along the so-called inner arc domain (Clark et al., 1983, 1990; Sandeman et al., 1995) or reararc (Kay et al., 2010; Salisbury et al., 2022), which is mostly restricted to the Eastern Cordillera. Contrasting to the main arc domain, profuse silicic magmatism along the inner arc domain is not related to subduction and is mostly peraluminous in composition (Clark et al., 1990). In both domains, the injection and ponding of hot, mantle-derived magmas in the lower crust induced high silicic magma productivity by promoting the generation of crustal melts as well as the favorable rheological conditions for magma differentiation (de Silva et al., 2006; de Silva & Gosnold, 2007; Salisbury et al., 2011; Kaiser et al., 2017; de Silva & Kay, 2018; Wörner et al., 2000, 2018). Such primitive magmas are derived from two distinct deep lithospheric mantle blocks beneath the eastern *versus* the western Andes, as documented by Carlier et al. (2005) in southeastern Peru, further enriching the element and isotope compositional variability of ignimbrite suites along the province.

In SE Peru, the most prominent examples of ignimbrite eruptive centers in the inner-arc domain are the Macusani and Picotani volcanic fields (Fig. 1; ca. 26-6.5 Ma, Sandeman et al., 1997). The Macusani Volcanic Field, the focus of our study, hosts igneous suites that are a reference example for the generation of large volumes of strongly peraluminous, rare-metal silicic magmatism (Barnes et al., 1970; Noble et al., 1984; Pichavant et al., 1988a, b; 2024a, b). Subordinated to volumetrically dominant ash-flow tuff in this locality is the so-called macusanite, a non-hydrated obsidian glass with extreme enrichment in incompatible lithophile elements (Li, Rb, Cs, Sn, U, B, and F) and an exotic mineralogy including andalusite, sillimanite, wollastonite, scapolite, and virgilite, a rare lithium aluminum silicate (Linck, 1926; French & Meyer, 1970; French et al., 1978; Pichavant et al., 1987, 1988a). Reports of macusanite are limited to boulders from specific ravines and valleys of glacio-fluvial origin and riverbeds, and a single report of *in situ*, coarse ash-sized, non-vesicular glass clasts interbedded in Miocene ignimbrite (Pichavant et al., 1987). Radiometric dating constrains the age of macusanite between ca. 8 Ma and 3 Ma (Barnes et al., 1970; Pichavant et al., 1987; Cheilletz et al., 1992; Poupeau et al., 1992, 1993). Previous authors inferred that the genesis of macusanite-like melts is related to extreme crystal fractionation products of dry, F-, B-, Li-, and P-rich, felsic peraluminous magmas (Pichavant et al., 1987, 2024a, b).

The recent discovery of a major Li resource at the Falchani Lithium Project (Fig. 2) by Macusani Yellowcake S.A.C., the Peruvian subsidiary of the Canadian company American Lithium, has broadened the attention to the Macusani Volcanic Field from an economic geology point of view. Falchani hosts indicated plus inferred resources of ~5 Mt Li (NI-43-101-compliant technical report; Nupen, 2019). More recently, American Lithium issued a press release announcing a 476 % increase in measured plus indicated Li resources (Clarke, 2023). The Falchani Lithium Project is located 750 km to the north of the so-called *Lithium Triangle of the Andes*, where Li resources are hosted by brines in salt flats, with a significant portion of the Li ultimately sourced from leaching of volcanic rocks of the Neogene Ignimbrite Province of the Central Andes (Meixner et al., 2020; López Steinmetz & Salvi, 2021). In contrast, at Falchani, the Li ore is hard-rock and hosted by a tuffaceous sequence called Lithium-rich Tuff, which has grades of ~0.3-0.4 wt % Li and, to a lesser extent, in the Upper Breccia and Lower Breccia units (Fig. 3; Nupen, 2019).

The occurrence of a large volcanogenic sedimentary lithium mineralization at Falchani raises questions about the petrogenetic specificities that led to the exceptional Li enrichment in the Li-ore units compared to other volcanogenic units in the Macusani Volcanic Field and, more broadly, among volcanic fields of the Neogene Ignimbrite Province of the Central Andes, in which lithium contents are typically < 50 µg/g (Meixner et al., 2020). Therefore, we present a geochemical and isotopic characterization of the Li-ore units of the Falchani Lithium Project, with a main focus on pre-eruptive magma petrogenesis. In addition, since Li-ore rocks at Falchani are variably altered to clay and zeolite minerals (Segovia-More et al., 2023), we also focused on the low temperature alteration process that led to post-depositional modifications of the primary igneous suite.

GEOLOGICAL SETTING

Tectonic framework of the Eastern Cordillera in southern Peru

The Eastern Cordillera is an east-directed retroarc fold-thrust belt exposing one of the longest Paleozoic metamorphic and magmatic belts in South America (Dorbath et al., 1991; Horton, 2018; Sundell et al., 2019; Gérard et al., 2021). A regional synthesis of the Proto-Andean evolution of the Eastern Cordillera of Peru by Chew et al. (2016) documents a series of polycyclic orogenies that shaped the western margin of Gondwana and dictated the initial framework for the subsequent Andean orogeny. This model describes the Eastern Cordillera as extending between the tectonic boundaries of Western Amazonia and allochthonous to parautochthonous terranes (Mišković et al., 2009). At the latitudes of southern Peru (south of ~14ºS), the Paleoproterozoic Arequipa terrane, which constitute the northernmost and oldest crustal domain of the Arequipa-Antofalla basement block (Loewy et al., 2004), represents a segment of a dismembered, Grenville-age orogenic belt that was first accreted to the Amazonian craton during the amalgamation of Rodinia in the Mesoproterozoic (Ramos, 2008, 2018).

The suture between the Arequipa terrane and the Amazonian craton has been a locus of magmatism, as well as of formation of extensional basins and repeated tectonic inversion (Ramos, 2018; Carlotto et al., 2023). It concentrated the extension during the middle Neoproterozoic breakup of Rodinia, which was aborted by the Permian Gondwanide orogeny heralding the complete assembly of Pangea. This suture also controlled the formation of a back-arc rift system, comprising half-grabens and pull-apart basins, during the initial stages of Pangea dismemberment in the Late Permian and Triassic. Syn-rift Triassic igneous and sedimentary deposits in Peru have been grouped under the Mitu Group, which comprises molasse facies and alkaline to subalkaline basalt and andesite (Spikings et al., 2016 and references therein).

The Eastern Cordillera developed during the Andean orogeny, mostly from selective tectonic inversion of pre-Cenozoic normal faults with its axis coinciding with that of the Triassic rift (Sempere et al., 2002), since the middle Eocene (Benjamin et al., 1987; Farrar et al., 1988; Allmendinger et al., 1997; Kley et al., 1997; Gillis et al., 2006; Buford Parks et al., 2023). The Eastern Cordillera in southern Peru encompasses three SE-oriented morpho-structural domains, which, from northeast to southwest, include the Cordillera de Carabaya, the Macusani Structural Zone, where the study area is located, and the Central Andean Backthrust Belt (Fig. 2a). The Macusani Structural Zone (Perez et al., 2016) was previously designated as a 'Late Hercynian' fold domain (Laubacher, 1978) or Pre-Cordillera de Carabaya (Kontak et al., 1990; Sandeman et al., 1997). It coincides with the northernmost segment of a late Permian Gondwanide orogenic belt recording multiphase, non-coaxial deformation of Permo-Carboniferous strata sealed by thick (>1 km) Triassic deposits of the Mitu Group (Mégard et al., 1978; Laubacher, 1978; Perez et al., 2016; Spikings et al., 2016). Three major Tertiary volcanic fields, represented geomorphologically by the Macusani (a.k.a. Quenamari; Audebaud, 1973; Rodríguez et al., 2021), Cayconi, and Picotani mesetas, are spatially related to intermontane topographic depressions, namely Macusani, Crucero, and Ananea-Ancocala (Kontak et al., 1990; Sandeman et al., 1997). Sandeman et al. (1997) grouped the Tertiary extrusive rocks in these volcanic fields under the Crucero Supergroup, and the small, petrographically similar, and broadly coeval silicic stocks and dykes under the Crucero Intrusive Supersuite.

The Macusani Volcanic Field

The Macusani Volcanic Field stands as the northernmost expression of the Neogene Ignimbrite Province of the Central Andes in the inner arc domain, Eastern Cordillera, and hosts the youngest Neogene eruptive system in the Macusani Structural Zone. The preserved ignimbrite sheets of the Macusani Volcanic Field delineate a perimeter with a broadly quadrilateral shape covering an approximate area of ~1300 km^2 (Fig. 2a; Cheilletz et al., 1992). The volcano-sedimentary sequence overlies Silurian-Devonian pelite and psammite, Carboniferous limestone, sandstone and shale, Triassic syn-rift red siliciclastic rocks and intra-plate alkaline basalt, Jurassic extrusive peralkaline rocks, and Cretaceous to Paleogene clastic sedimentary series. The outcropping volcanic and volcano-sedimentary strata include restricted exposures of rhyodacitic tuff and basaltic andesite of the Oligocene-Miocene Picotani Group and volumetrically dominant rhyolitic rocks of the Macusani Formation, which represents the youngest formation of the middle- to late-Miocene Quenamari Group (Sandeman et al., 1997).

The Macusani Formation is a sequence of whitish-gray, poorly stratified, unwelded, crystal-rich, rhyolitic ash- and lapilli-flow tuff (Sandeman et al., 1997). Erosional unconformities separate the Macusani Formation from the underlying Paleozoic-Mesozoic basement rocks and Oligocene-Miocene Picotani Group. The original thickness of the Macusani Formation is unknown due to the erosion of its uppermost section. In the eastern margin of the volcanic field, where the youngest units are exposed, the thickness ranges from 340 to 440 m (Cheilletz et al., 1992). ^{40}Ar/^{39}Ar biotite dates through five stratigraphic sections revealed two brief eruption episodes recorded by two intraformational members at 10 ± 1 and 7 ± 1 Ma (Cheilletz et al., 1992). There have been several attempts to subdivide the Macusani Formation into different sub-units. López (1996) identified three intra-formational members within the Macusani Formation separated by erosive unconformities that are continuously mappable at a regional scale, which from bottom to top are Chacacuniza, Sapanuta, and Yapamayo (Fig. 2). Li (2016) also attempted to subdivide the Macusani Formation into three sub-units, designated as Units A, B, and C based on field and drill-core observations in the NE portion of the Macusani Volcanic Field. However, both sub-divisions are not supported by accompanying geochronological data.

The Macusani Formation comprises strongly peraluminous felsic volcanogenic series characterized by a strong enrichment in lithophile incompatible elements, such as Li, Rb, Cs, Be, B, Sn, F, P, and U (Noble et al., 1984; Pichavant et al., 1988b). Mineralogically, it chiefly consists of quartz, sanidine, plagioclase, biotite, and muscovite, minor amounts of tourmaline, spinel, cordierite, and sillimanite, and accessory ilmenite, apatite, monazite, and zircon (Pichavant et al., 1988a).

More recently, Nupen (2019) reported white, very fine-grained, tuffaceous rocks with Li contents up to 0.4 wt %, namely the Lithium-rich Tuff, and transitional Li-rich breccias located in the central area of Macusani Volcanic Field. The Lithium-rich Tuff is a 50 to 140 m-thick unit sandwiched between the 10-20 m-thick Upper Breccia and the <175 m-thick Lower Breccia units (Fig. 3a). According to Nupen (2019), the Lithium-rich Tuff comprises finely laminated to massive facies, which were deposited in a crater lake volcano-sedimentary environment. Mica crystal clasts in the Lithium-rich Tuff yielded ^{40}Ar/^{39}Ar plateau dates in the range from 8,979 ± 73 ka to 8,717 ± 44 ka (Sanandres-Flores, 2024).

Silicic stocks and dykes of the Crucero Intrusive Supersuite are exposed across the Macusani Volcanic Field. These include the biotite-cordierite monzogranitic Quebrada Centilla and Ninahuisa stocks and the Revancha dyke of the Picotani Intrusive Suite and the two-mica syenogranitic Chacacuniza stock and Nevado Ollo Quenamari and Cayo Orjo plugs of the Quenamari Intrusive Suite (Sandeman et al., 1997).

MATERIALS AND METHODS

Sampling: strategy and lithotypes

A list of the analyzed samples and their locations and field descriptions is provided in the Supplementary Table S1. Rock samples were collected from rock outcrops and drill cores. Twenty-nine samples (including duplicates) of tuff and intrusive rocks were selected for investigation of their major and trace element compositions. Additionally, fourteen of these samples were also analyzed for isotope (Sr, Nd, Pb) composition. With a main focus on the Lithium-rich Tuff unit, the selection criteria included petrographic, geographic, and stratigraphic diversity. Most of the analyzed samples were collected from the Falchani Lithium Project (*n* = 25), which encompasses both the Falchani and Ocacasa 4 concessions situated in the central portion of the volcanic field (Fig. 2a-b). Additional samples were obtained from the Quelcaya (*n* = 3**)** and Cerro Sumpiruni (*n* = 1) areas. The studied samples were divided into six lithotypes as described below.

Upper Breccia

The studied samples of Upper Breccia (*n* = 4) were collected from the Falchani concession (Fig. 2). This unit includes altered, brecciated, volcaniclastic facies located stratigraphically above the Lithium-rich Tuff (Fig. 3a). The rocks in the Upper Breccia are mostly non-cohesive, clayey, and white to grayish-white in color (Fig. 3b). The breccia is predominantly clast-supported, with angular clasts ranging in size between 2 and 5 cm. Scarce medium to coarse ash-sized dark mica, K-feldspar, and translucent quartz crystal fragments within clasts are matrix-supported. The samples are pervasively altered to dioctahedral smectite and zeolites (Segovia-More et al., 2023).

Lithium-rich Tuff

The analyzed Lithium-rich Tuff samples were obtained from the Ocacasa 4 (n = 2) and Falchani (n = 15) concessions (Fig. 2). It comprises finely laminated—with alternating white/gray laminae—or locally massive volcanic mudstone with a characteristic white color (Fig. 3c-d). The Lithium-rich Tuff is mostly cohesive and massive, except for the occurrence of cavernous, globular, cm-scale concretions that are aligned parallel to the general rock lamination in some samples (Fig. 3c). The lamination is mostly strongly folded and contorted, including disorganized, asymmetric, slump structures (Fig. 3c) indicating pre-lithification, sub-aqueous deformation of soft sediments. Since it is a pyroclastic-rich, resedimented deposit, it is best classified as a tuffaceous mudstone (McPhie et al., 1993). Fairly abundant interlayered dark mica crystal clasts up to 3 mm in size stand in the white rock (Fig. 3e). Compositionally, these micas are zinnwaldite and lepidolite, and often the crystal clasts include a core of zinnwaldite and a thin rim of lepidolite (see compositional and textural data of the Li-F micas in Torró et al., 2023). The other minerals in the Lithium-rich Tuff are very fine grained and comprise feldspar, plagioclase, K-feldspar, and variable proportions of kaolinite subgroup (kaolinite ± halloysite) and zeolite minerals (Segovia-More et al., 2023).

Lower Breccia

The studied samples of Lower Breccia were collected from the Falchani (n = 1) and Ocacasa 4 (*n* = 1) concessions (Fig. 2). This unit consists of brecciated volcaniclastic facies located stratigraphically below the Lithium-rich Tuff. The pervasive alteration of the samples to dioctahedral smectite and zeolites (Segovia-More et al., 2023) has obliterated most primary textures and led to distinctive low hardness and clayey textures. Scarce, medium ash-sized biotite crystal clasts are observed very locally.

Ash-flow tuff

The ash-flow tuff samples in our study are divided into pre- and post-Li-ore units according to their stratigraphic position. Pre-Li-ore ash-flow tuff occurs stratigraphically below the Lower Breccia and was sampled in the Falchani concession ($n = 2$). Post-Li-ore ash-flow tuff occurs stratigraphically above the Upper Breccia unit and was sampled in the Falchani ($n = 2$) and Ocacasa 4 ($n = 2$) concessions and in the Quelcaya area ($n = 2$; Fig. 2). The ash-flow tuff samples are poorly sorted and crystal-rich, exhibiting a white, aphanitic matrix and variable proportions of coarse lapilli-sized juvenile clasts. Their characteristics align closely with those described in ash-flow tuff of the Macusani Formation by Sandeman et al. (1997).

Quenamari Suite granite

This term refers to sampled intrusive stocks belonging to the middle- to late Miocene Quenamari Suite of the Crucero Intrusive Supersuite (Sandeman et al., 1997). The studied samples include a stock in the Falchani concession ($n = 1$) and a dyke in the Quelcaya area ($n = 1$; Fig. 2). The samples consist of leucocratic, medium- to coarse-grained, tourmaline-bearing, two-mica granites. They show porphyritic and hypidiomorphic textures and a white and aphanitic groundmass. Coarse- to very coarse-grained K-feldspar phenocrysts occur along fine- to medium-grained quartz phenocrysts and medium- to very fine-grained biotite, muscovite, and rare tourmaline phenocrysts.

Picotani Suite granite

This term refers to a granite sample that belongs to the Oligocene-Miocene Picotani Suite of the Crucero Intrusive Supersuite (Sandeman et al., 1997). The studied sample (*n* = 1) was collected from the Ninahuisa Stock (Fig. 2) and is a leucocratic, medium-grained, cordierite-biotite granite with porphyritic and hypidiomorphic textures and a pinkish-brown aphanitic groundmass. The most notable textural feature of the sample is the conspicuous occurrence of K-feldspar megacrysts that are up to 15 cm long. Coarse-grained quartz and medium- to very fine-grained biotite phenocrysts are also abundant, while medium- to very coarse-grained (up to 20 mm), greenish brown, pinitized cordierite phenocrysts appear in lesser amounts.

Sample preparation

For bulk geochemical analyses, weathered parts of rock samples were removed by cutting with a diamond saw. The cut samples were then dried at 70 °C overnight and subsequently crushed with a jaw crusher until a fine powder was obtained. A representative fraction of about 10 g of the crushed rock samples was separated through rotary splitters and then manually powdered to <50 µm using an agate mortar and pestle.

The Loss On Ignition (LOI) was analyzed using a programmable Carbolite furnace with a Eurotherm 301 temperature controller. Approximately 3.5 g of powdered sample were heated in a ceramic crucible at a heating rate of 15 °C/min, and then subjected to two thermal treatments: i) 24 hours at 100 °C to volatilize water (H_2O) within rock porosity; and ii) 48 hours at 950°C to release structurally-bounded water (OH^-, H_2O). The weight changes of each sample were registered before and after both thermal treatments.

A 2 g fraction of each thermally treated sample was utilized to prepare fused beads (homogeneous glass). A homogeneous mixture of 1:5 of thermally treated sample and flux (66.67% $Li_2B_4O_7$, 32.83% $LiBO_2$, 0.5% LiBr) was introduced into a Katanax K1 Prime Electric Fluxer with a platinum crucible and a cylindrical standard sample holder of 16 mm in diameter and 2.5 mm in height.

Whole-rock element geochemistry

The whole-rock major and minor element contents (SiO_2, TiO_2, Al_2O_3, Fe_2O_{3tot}, MnO, MgO, CaO, Na_2O, K_2O, Cr_2O_3, and NiO) were determined by X-ray fluorescence (XRF) using a Bruker-S8 Tiger available in the Centro de Caracterización de Materiales of the Pontifical Catholic University of Peru (CAM-PUCP). The analyses were conducted on the fused beads. Calibration was based on the standards G-1 (USGS), RGM-2 (USGS), JA-3 (Japan GS), and JB-3 (Japan GS). The data are reported on a LOI-free basis. The limits of detection for each element were determined to be in the range of 20 to 80 ppm.

The trace element contents were determined in the same fused beads used for XRF analyses by means of laser ablation inductively coupled plasma mass spectrometry (LA-ICP-MS). Measurements were performed with an Excimer 193 nm (ArF) GeoLas (Coherent) laser system coupled to a Perkin Elmer Nexion 2000 quadrupole mass spectrometer at ETH Zürich. Measurements were conducted using a laser repetition rate of 10 Hz and a laser energy density of ~10 J/cm^2 on the sample surface. The ablation aerosol was mixed in the in-house built ablation cell with carrier gas consisting of helium (~1 L/min). The ablated aerosol was then mixed with argon make-up gas and homogenized by flushing through an in-house built squid device before introduction into the plasma torch. An analytical scheme of 30 s recording gas blank and 40 s of target ablation was implemented following standard-sample bracketing procedure. Synthetic glass NIST SRM610 (Jochum et al., 2011) was analyzed every 15 unknowns with a spot size of 40 μm and used as primary reference material for normalization and instrumental drift correction. Fluxer blank was ablated using a spot size of 110 μm to correct for matrix effects on the glass beads. Secondary standard USGS BCR-2 (Raczek et al., 2001) was also analyzed with a spot size of 110 μm to test the accuracy and reproducibility of the analysis (ca. in the range of 2%–10% for the elements of interest). Three individual measurements per sample were made following the same parameters as for blanks and secondary standards. Data reduction was carried out in the MATLAB-based SILLS program (Guillong et al., 2008). XRF results (SiO_2 content) were used as an internal standard.

Whole-rock B and Li contents were determined at ALS Laboratories (Vancouver, Canada) by sodium peroxide fusion followed by ICP-MS analysis using the ME-ICP82b analytical package. Whole-rock Cl and F contents were analyzed in the same laboratory by KOH fusion and ion chromatography using the Cl-IC881 and F-IC881 analytical packages, respectively. The whole-rock major and trace element contents are provided in the Supplementary Table S2.

Whole-rock isotope geochemistry

Lead isotopic compositions were measured on powdered samples using a Thermo Neptune Plus Multi-Collector ICP-MS in static mode at the University of Geneva following the method described in Chiaradia et al. (2020). External reproducibility (1σ) of the Pb isotope analyses assessed using the NIST SRM 981 is 0.11% for $^{206}Pb/^{204}Pb$, 0.12% for $^{207}Pb/^{204}Pb$, and 0.20% for $^{208}Pb/^{204}Pb$.

Whole rock Sr and Nd isotopic compositions were obtained in GET-OMP, Toulouse University (France), using the Thermo Scientific TRITON+ solid source mass spectrometer, following Li et al. (2011, 2012) and Labou et al. (2020) procedures. Before measurement, about 100 mg of whole rock powder was weighed in a Teflon beaker and dissolved in a mixture HF/HNO_3 1:1. After dissolution, samples were diluted in 1 ml, 2% HNO_3 and Nd/Sr were extracted from the matrix (2N HNO_3) using a combination of Sr-Spec and Thru-spec Eichrom resins. Mixed Sr and REE were loaded on a Re filament and run sequentially (first Sr then Nd) using a double Re filament protocol. The monitoring of the interferences of ^{87}Rb and ^{144}Sm was performed according to the protocol of Li et al. (2012) and the quality and reproducibility of the measurements were controlled using a sequential measurement of isotopic standards (SRM 987 and JNdi), doped isotopic standards (NBS 987+ Rb and JNdi + Sm), and laboratory-dedicated Sr+REE artificial solutions. Standard reproducibilities are 0.710270 ± 20 (n=47) for SRM-987 and 0.512099 ± 7 (n=22) for JNdi and fall within the recommended values. Measured blanks are 300 pg for Sr and 7 pg for Nd. $^{87}Sr/^{86}Sr$ and $^{143}Nd/^{144}Nd$ ratios were normalized against $^{86}Sr/^{88}Sr = 0.1194$ and $^{146}Nd/^{144}Nd = 0.7219$ respectively, after corrections from isobaric interferences using $^{87}Rb/^{85}Sr = 0.387041$ on ^{87}Sr and combination of $^{147}Sm/^{149}Sm = 1.08583$ and $^{147}Sm/^{144}Sm = 4.87090$ on ^{144}Nd.

The whole-rock isotopic compositions are provided in Table 1. The isotopic ratios were corrected for an age of 8.9 Ma based on new $^{40}Ar/^{39}Ar$ dates on mica crystal clasts from the Lithium-rich Tuff (Sanandres-Flores, 2024).

RESULTS

Major element geochemistry

The Lithium-rich Tuff, macusanite, and ash-flow tuff have relatively homogeneous total alkalis (Na_2O+K_2O) and SiO_2 contents (Fig. 4a; Table S1) and display subalkaline rhyolitic compositions (Fig. 4b). The samples of Li-ore with higher LOI values, particularly those of the Upper and Lower Breccia, are scattered outside the main data cluster due to a depletion in SiO_2 and alkalis (Fig. 4a), specifically in K_2O (Figs. 5a, S1), probably representing a non-magmatic signature as discussed below.

All the analyzed samples are strongly peraluminous with A/CNK values between 1.1 and 2.8 (Fig. 4c). In the B-A diagram of Debon & Lefort (1983), all the Li-ore samples plot mostly above the felsic peraluminous field due to their very low B (i.e., Fe+Mg+Ti) and extremely high A (i.e., Al-(K+Na+2Ca)) values, similar to the macusanite and highly-evolved rare-metal granites and volcanic rocks (Fig. 4d). In contrast, most ash-flow tuff from the Macusani Formation samples have A-B values comparable to those of muscovite-biotite and muscovite granites. The geochemical similarity between the magmatic rocks in the Macusani Volcanic Field and rare-metal and peraluminous granites had been previously noted by Pichavant et al. (2024a).

The Li-ore samples exhibit very high F contents (1.05-1.98 wt %), which are up to 30x above the average values reported for the upper continental crust (Figs. 5a, S1). The P_2O_5 contents (0.2-0.8 wt %) are also high, up to five times higher than in the upper continental crust. Other minor elements (TiO_2, Fe_2O_{3tot}, MnO, MgO, and CaO) collectively add to 1.13 wt %, on average. The MgO contents are particularly low, typically below the detection limit at 0.02 wt %. Compared to the ash-flow tuff from the Macusani Formation, the Li-ore rocks are enriched in Al_2O_3, P_2O_5, and MnO and depleted in TiO_2, K_2O, CaO, MgO, and Fe_2O_{3tot}. In contrast, the Li-ore units, and particularly the samples of Lithium-rich Tuff with LOI < 2.7 wt %, show similar compositions to macusanite in terms of most minor elements except for a general depletion in Na_2O (Fig. 5a).

Trace element geochemistry

The Lithium-rich Tuff exhibits strong enrichment in Li (2920-4160 µg/g [ppm]; median = 3540 ppm) and Rb (1139-2177 ppm; median = 1502 ppm), mostly at the thousands of ppm level, compared to the upper continental crust. Other elements that are also enriched in the Lithium-rich Tuff compared to the upper continental crust include B, Cs, Sn, and Be, mostly at the hundreds of ppm level, and Nb, Ta, and U, mostly at the tens of ppm level (Figs. 5a, S2; Table S2). In contrast, the Lithium-rich Tuff is depleted relative to the upper continental crust in Cl, Ba, Zr, Sr, and Th. A similar geochemical footprint is observed for the Upper Breccia and Lower Breccia, which are strongly enriched in Li (780-2890 ppm; median = 1285 ppm), B (600-2100 ppm; median = 1600 ppm), Cs (656-1822 ppm; median = 1356 ppm), and Rb (1139-2177 ppm; median = 1095 ppm), mostly at the thousands of ppm level, compared to the upper continental crust. In addition, they are enriched in Cl, Sn, and Be, mostly at the hundreds of ppm level, and Nb, Ta, and U, mostly at the tens of ppm level, and depleted in Zr, Ba, Sr, and Th, relative to upper continental crust values (Figs. 5a, S2; Table S2).

In terms of minor and trace elements, the Li-ore is strongly enriched in volatiles such as halogens (F, Cl) and B and other incompatible lithophile elements such as Li, Be, and some LILE (Cs, Rb) and HFSE (Nb, Ta, Sn, W) compared to the ash-flow tuff from the Macusani Formation (Fig. 5a, S2). In contrast, the Li-ore is depleted in other HFSE (Zr, Hf, Th) and LILE (Ba, Sr) and show equivalent Pb compared to the ash-flow tuff. As with major elements, the trace element contents in the Li-ore units, in particular the Lithium-rich Tuff, are similar to those of macusanite, particularly in terms of F, Li, Be, Rb, Sr, Nb, Zr, Hf, Cs, and Ba, with lower contents of B and U and higher contents of Ta and Pb.

The Li-ore samples yield individual REE and Y values that are ~1 to 20 times enriched relative to chondrite C1 values (Fig. 5b). The chondrite-normalized REY (lanthanides + Y) patterns have negative slopes ($(La/Sm)_{CN}$ = 2.3-3.6), $(Sm/Yb)_{CN}$ = 1.2-2.9) and negative Eu anomalies ($(Eu/Eu^*)_{CN}$ = 0.11-0.34). Most Li-ore analyses show ΣREE and Y contents that are intermediate between those of Macusani Formation ash-flow tuff and macusanite (Fig. 5b). The chondrite-normalized REY patterns of Li-ore units closely resemble those of macusanite except for slightly higher La/Sm and less pronounced Eu negative anomalies. The analyses of ash-flow tuff yield higher $(La/Sm)_{CN}$ and $(Sm/Yb)_{CN}$ and lower to non-existent Eu negative anomalies relative to the Li-ore units.

Mass balance

Mass balance and relative element gains and losses due to metasomatism, principally post-depositional alteration, were addressed with isocon diagrams (cf. Grant, 1986, 2005) for Upper and Lower Breccia (Fig. 6a) and Lithium-rich Tuff (Fig. 6b). Given that the alteration minerals identified in the Li-ore samples comprise hydrated phases (i.e., kaolinite, zeolite, smectite; Segovia-More et al., 2023), the LOI values can effectively be used as a monitor for the degree of alteration. The least altered composition (C_O) was calculated as the average element contents of seven Lithium-rich Tuff samples with LOI < 2.7 wt %. In the absence of low-LOI Upper Breccia and Lower Breccia samples, and given the similarity between their trace-element patterns and those of the Lithium-rich Tuff (Fig. 5a-b), a unique protolith composition was assumed. The use of pre- or post-lithium ore ash-flow tuff as C_O was discarded due to the above-described systematic geochemical differences with Li-ore samples. Alteration quantification (C_A) was conducted on samples with LOI values between 1.68 and 13.5 wt % including five Lithium-rich Tuff, four Upper Breccia, and two Lower Breccia samples. Isocon lines were established under the assumption that TiO_2 remained immobile during post-depositional alteration processes. This assumption is common in mass balance analyses applied to rocks that have undergone hydrothermal alteration and/or weathering (Grant, 2005) due to the very limited mobility of titanium in these environments (e.g., Hill et al., 2000; Ulrich & Heinrich, 2002). The results indicate a total mass loss of 3.9 wt % in the Lithium-rich Tuff and of 6.5 wt % in the Upper and Lower Breccia. The isocon diagrams indicate general gains in Ca, Mg, Mn, Zn, As, Cl, Sr, Cs, B, and Bi, and losses in SiO_2, Na_2O, K_2O, Li, Rb, W, and F. According to our results, Al_2O_3, Fe_2O_3, Th, Nb, Ta, and Sn were mostly conserved during alteration. Zirconium and Y remained immobile except for a strong gain in a sample of Breccia (2021-MAC-051). Lithium losses were more pronounced in the samples of Breccia than in the samples of Lithium-rich Tuff.

Isotopic data (Pb, Sr, and Nd)

Initial isotope ratios have been recalculated at 8.9 Ma except for the granite sample from the Picotani Suite, which was recalculated at 24 Ma (Table 1). Lead isotope compositions of the analyzed samples exhibit a high degree of homogeneity, with $^{206}Pb/^{204}Pb_{(t)}$, $^{207}Pb/^{204}Pb_{(t)}$, and $^{208}Pb/^{204}Pb_{(t)}$ ratios in the range of 18.7861–18.9191 (avg. = 18.8625 ± 0.0024, 2σ), 15.6838–15.7011 (avg. = 15.6907 ± 0.0020), and 38.8559–38.9753 (avg. = 38.9405 ± 0.0050), respectively (Fig. 7a, c). Excluding the Lithium-rich Tuff sample 2021-MAC-031, which is a clear outlier, $^{87}Sr/^{86}Sr_{(t)}$ ratios are between 0.715426 and 0.728031 (avg. = 0.721278 ± 0.000005), and $^{143}Nd/^{144}Nd_{(t)}$ ratios are in the narrow range between 0.512080 and 0.512186 (avg. =

0.512171 ± 0.000007; Fig. 8a), which correspond to negative ε_{Nd}^{t} values ranging from -10.3 to -8.0 (avg. = -8.7). The sample 2021-MAC-031 yielded significantly lower $^{87}Sr/^{86}Sr_{(t)}$ (0.703868) and higher $^{143}Nd/^{144}Nd_{(t)}$ (0.512990) ratios and ε_{Nd}^{t} (7.4) values. Most of the new data plot within the Pb-isotope compositional range defined by macusanite, which is characterized by a larger dispersion than the analyzed samples (Fig. 7a, c). While the new data show similar $^{143}Nd/^{144}Nd$ as macusanite, the latter is characterized by much higher $^{87}Sr/^{86}Sr$ values (Fig. 8b).

DISCUSSION

Nature of the magmatic component in the lithium ore units

Given the alteration features documented in Li-ore rocks from the Falchani Lithium Project (Segovia-More et al., 2023), immobile elements will be employed to approximate the nature of the magmatic protolith. Elements such as Al, Ti, Zr, Y, Nb, and Ta are relatively immobile upon low-temperature hydrothermal alteration and weathering and hence could be used as proxies for the primary petrogenetic processes (Winter, 2014; Rollinson & Pease, 2021). However, it should be noted that some of these elements have been demonstrated to mobilize under certain hydrothermal conditions (e.g., Zr in F-rich hydrothermal systems, Rubin et al., 1993) and therefore the conclusions drawn from these proxies should be considered with a degree of caution. In our isocon diagrams, Al, Ti, Zr, Nb, and Ta remained mostly unchanged and only one sample of breccia showed a significant enrichment in Zr and Y (Fig. 6). In the Zr-Al_2O_3-TiO_2 provenance discrimination plot for weathered rocks of García et al. (1994), most of the Lithium-rich Tuff, Upper Breccia, and Lower Breccia datapoints plot in the field of strongly peraluminous granites, akin to macusanite and ash-flow tuff from the Macusani Formation (Fig. S3).

The Lithium-rich Tuff and Upper and Lower Breccia have lower Nb/Ta and Zr/Hf than the CHARAC (CHArge-and-RAdius-Controlled) range (Fig. 9a), indicating that elements of similar charge and radius did not behave coherently as expected in pure, depolymerized silicate melts (Bau, 1996; Schmidt et al., 2014). This feature is common in peraluminous, rare-metal-rich granitic rocks (Fig. 9a) and is attributed to either interaction with ligand- (e.g., F) rich, acidic, and reduced magmatic fluids (Ballouard et al., 2016) or fractional crystallization (Linnen & Keppler, 1997, 2002). The Lithium-rich Tuff and Upper Breccia exhibit a composition similar to several Variscan rare metal-rich granites and highly evolved volcanic equivalents in terms of Nb, Ta, Nb/Ta, Rb, and Li signatures (Michaud et al., 2021; Fig. S4). In contrast, the samples of ash-flow tuff plot in the biotite, biotite-muscovite, and muscovite Variscan granites compositional fields. Finally, the analyses of Li-ore rocks systematically plot in the Li-mineralized pegmatite field in the Mg/Li *versus* La/Ta diagram of Shaw et al. (2022), while all the other analyzed samples plot in the “unmineralized pegmatites and granites” field (Fig. 9b).

In summary, while the Li-ore, ash-flow tuff from the Macusani Formation, and related intrusive rocks all share geochemical signatures with peraluminous granitic systems, the composition of the Lithium-rich Tuff is close to that of the most fractionated lithologies observed in these systems. Additionally, Torró et al. (2023) described contrasting, more evolved compositions for mica crystal clasts in the Lithium-rich Tuff (zinnwaldite and lepidolite) relative to micas in other Neogene volcanic and intrusive rocks from the Macusani Volcanic Field, which approximate the compositions of siderophyllite and muscovite. The only exceptions are mica crystals in macusanite (Pichavant et al., 1988a), which plot near the compositional field defined by zinnwaldite from the Lithium-rich Tuff (Torró et al., 2023). This further emphasizes the identification of parental magmas to the Lithium-rich Tuff with highly evolved, peraluminous rhyolitic melts.

Source regions of parental magmas to the Lithium-rich Tuff

The petrogenesis of the Macusani Formation ash-flow tuff and macusanite has been previously explained by Pichavant et al. (1987; 1988a, b; 2024a) in terms of batch melting of isotopically heterogeneous crustal rocks dominated by pelitic metasedimentary lithologies. The low f_{H2O}/f_F recorded in biotite, tourmaline, and apatite, as well as the absence of muscovite in the early magmatic stage indicate partial melting under H_2O-undersaturated conditions, with a_{H2O} internally controlled by dehydration melting of F-rich muscovite and incipient melting of biotite (Pichavant et al., 1988a, b). The relatively high anorthite content (>30 % An) and the strong enrichment in Sr, Ba, and La in cores of plagioclase from this early magmatic stage have been interpreted by Pichavant et al. (2024a) as evidence of interaction between crustal melts and potassic to ultrapotassic (K-UK), mantle-derived magmas at the source level. The role of crustal and mantle components is discussed below by combining literature and newly acquired isotopic data.

Pelitic rocks from the Andean basement that are suitable proxies for the compositions of crustal end-members include Proterozoic and Paleozoic paragneiss from the Puna plateau and Sierras Pampeanas (DIGIS Team, 2023), and Ordovician metapelite rocks of the Sandia Formation exposed in the Macusani Structural Zone (Harlaux et al., 2021). The selected paragneiss samples are located over 1000 km to the south of the Macusani Volcanic Field (Fig. 1), yet they exemplify an ancient Andean crustal end-member of meta-sedimentary origin with elevated Rb/Sr ratios. The only comparable lithologies of similar age in the Eastern Cordillera of southern Peru are the poorly studied gneissic rocks of the pre-Cambrian Iscaybamba metamorphic complex in the Cordillera de Carabaya, for which no Sr-Nd isotopic data are available (Laubacher, 1978; Sánchez & Zapata, 2003). On the other hand, Paleozoic metapelite rocks in the Macusani Structural Zone have been proposed as a source component of granites from the Picotani Suite in the San Rafael and Santo Domingo intrusive complexes (Harlaux et al., 2021). Noteworthy, recent studies have highlighted that partial melting of felsic meta-igneous (orthogneiss) rocks that are initially enriched in both F and Li can evolve into rare-metal granite compositions (Ballouard et al., 2023a). However, Ordovician, Silurian-Devonian, Carboniferous, Permian, and Triassic granitoids located between 12-14°S (Reitsma, 2012; Martínez et al., 2019) are too rich in radiogenic Nd to be considered as possible end-members in the context of our study case (Fig. 8b).

Despite the Macusani Volcanic Field is proximal to the northern domain of the Arequipa-Antofalla basement block (Fig. 1), the Lithium-rich Tuff and other Neogene volcanogenic and intrusive units in Macusani exhibit Pb-Nd isotope ratios that are consistent with those of the Mesoproterozoic, central—particularly the Quebrada Choja— crustal domain of this basement block (Figs. 7b, d, 8d). The Sm/Nd T_{DM} ages calculated for Macusani Formation rocks extend from ca. 1.5 Ga to values as high as 3.8 Ga (Fig. 8d; Table 1). This marked dispersion is attributed to an artifact resulting from lower $(La/Sm)_{CN}$ values and higher Sm/Nd ratios in the more fractionated rocks. The depletion in LREE during magmatic differentiation in Macusani magmas has been explained by Pichavant et al. (1988b). The least fractionated Lithium-rich Tuff sample yields a Sm/Nd T_{DM} age of ca. 1.5 Ga, which agrees with a metapelitic source ultimately derived from juvenile Mesoproterozoic crust. Nevertheless, a mixed metapelitic source including a mixture of detrital material from various—older and younger—ages giving a coincidental model age of 1.5 Ga cannot be discarded (see Couzinié et al., 2019).

With regard to the mantle-derived end-member, the most suitable candidates are the Cenozoic K-UK mafic intrusions exposed in the Eastern Cordillera. These lithologies were interpreted by Carlier et al. (2005) as derived from hybridized magmas consisting mainly of enriched mantle-derived melts and a volumetrically minor depleted asthenospheric mantle component. Given the absence of late Miocene—i.e., the age of the Macusani Formation—equivalents in the Macusani Structural Zone, a late Miocene (7.51 ± 0.05 Ma; $^{40}Ar/^{39}Ar$ phlogopite date, error 2σ) olivine minette from the Eastern Cordillera (Carlier et al., 2005) located ~200 km to the northwest of the Macusani Volcanic Field (Fig. 1) was selected as the mantle-derived end-member.

To assess the relative contributions of continental crust- and mantle-derived melts in magmas that were parental to the Lithium-rich Tuff and other Neogene volcanogenic and intrusive materials in the Macusani Volcanic Field, we have developed a simple binary mixing model based on Sr-Nd isotope relations (Fig. 10). Noteworthy, the calculated Rb-Sr isochron age of 9.9 ± 1.6 Ma for the Lithium-rich Tuff (Fig. 8c) is virtually equivalent to the $^{40}Ar/^{39}Ar$ mica dates for the same rocks (ca. 8.9 Ma; Sanandres-Flores, 2024), indicating that the Sr isotope ratios have not been disturbed during post-eruptive events. The produced mixing model reproduce the Sr-Nd composition of the studied rocks as containing ~5-25% of mantle contribution and ~75-95% of paragneiss and/or metapelite contribution. We note that defining crustal end-members as the average values of rocks that exhibit significant scatter in terms of Sr-Nd isotope ratios (Figs. 8b, 10) may be an oversimplification. Consequently, the obtained percentages in the mixing model should be regarded as approximations.

The mixing model would suggest that most Lithium-rich Tuff samples record slightly higher mantle contributions compared to other Neogene igneous rocks in the Macusani Volcanic

Field (Fig. 10). The relatively high dispersion of ^{88}Sr/^{87}Sr ratios in the volcanogenic material of the Macusani Formation can also be explained either by different melting mechanisms and kinetics (Farina et al., 2014) and/or isotopically heterogeneous crustal protoliths (e.g., Pichavant et al., 1988b; Guillot & Le Fort, 1995; Romer et al., 2014) combined with a lack of complete ^{87}Sr/^{86}Sr homogenization during metamorphism and anatexis (Wolf et al., 2019; Pichavant et al., 2024b).

Finally, the Neogene volcanic rocks from the Macusani Volcanic Field, including those from the Li-ore units, exhibit elevated ^{87}Sr/^{86}Sr$_{(t)}$ ratios relative to other Neogene to Quaternary ignimbrite rocks in the Central Andes (Fig. 8b). This indicates a greater proportion of crustal component and/or the contribution of crustal rocks with high Rb/Sr ratios and strongly supports that the felsic nature of the igneous rocks from the Macusani Formation is at least in part the result of a distinctively elevated crustal contribution to parental magmas.

Controls on the composition of Li-ore

As outlined above, the Lithium-rich Tuff displays a notable compositional similarity with macusanite, a characteristic that distinguishes it from other volcanogenic materials within the Macusani Formation. This and the exclusive presence of magmatic Li-F micas (zinnwaldite and lepidolite, Torró et al., 2023) suggest that the petrogenesis of the volcanogenic material in the Lithium-rich Tuff might be, to some extent, comparable to that of peraluminous rare metal-rich magmas in general and of macusanite in particular. The petrogenesis of the Lithium-rich Tuff will therefore be first discussed in the context of previously asserted petrogenetic processes for macusanite. Since the Lithium-rich Tuff is a volcanogenic sedimentary rock and not an obsidian, compositional changes due to physical segregation during pyroclastic and sedimentary processes (cf. Cas & Wright, 1988; McPhie et al., 1993) will also be discussed. Finally, the potential impact of fluid-mediated processes in the composition of the Li-ore samples is evaluated.

Magma differentiation

According to Pichavant et al. (1988a, b), an early crystallization stage, which is recorded as early phases in ash-flow tuff of the Macusani Formation, occurred at ~800 °C and < 5-7.5 kbar at or near the magma source region. This event was followed by the main crystallization stage, triggered by a rapid ascent of the magmas and consequent drop in temperature and pressure to ~650 °C and 1.5 kbar. In this frame, macusanite would have resulted from crystal fractionation of interstitial liquids in magmas parental to the ash-flow tuff from the driest and F-, B-, Li-, and P-richest magma batches (Pichavant et al., 1987). From mineral/melt partition coefficients determined directly on Macusani volcanics, Pichavant et al. (2024a) modeled chemical fractionation in Macusani magmas. The model was based on the composition of matrix glass and mineral abundances in ash-flow tuff (Pichavant et al., 1988a) and on alternative scenarios created by arbitrarily varying the proportion of phenocrysts and/or slightly adjusting partition coefficients and the initial composition of the melt. By doing so, the authors constrained that the trace element contents in macusanite can be reproduced for 50-70% crystallization of matrix glass in the ash-flow tuff.

We reproduced the fractional crystallization models of Pichavant et al. (2024a) using Rb as a differentiation index, the composition of the least-evolved interstitial glass in ash-flow tuff (MA85-4, MA85-7 in Pichavant et al., 2024a) as the initial melt, and the six different modal proportions of phenocrysts considered by these authors (Figs. 11-12; model parameters provided in Fig. 11 caption). We have labeled this model set as Model 1. In addition, we produced additional fractional crystallization models considering a range of various plausible scenarios, incorporating varying initial compositions of the differentiating melt within the petrogenetic model of Pichavant et al. (2024a). To encompass this diversity, we modeled fractional crystallization from i) the most evolved glasses in ash-flow tuff (glass inclusions in sample MH1 in Pichavant et al., 2024a) as a potential non-cogenetic melt (cf. Pichavant et al. 1988a, b) (Model 2); and ii) from a theoretical initial melt resulting from magma hybridization of the respective initial melts with increasing contributions of mantle-derived melts (Model 3; Figs. 11-12). Model 3 was applied to both the least-evolved interstitial glass (Model 3a) and the most evolved glasses (Model 3b) in ash-flow tuff.

Model 3 stems from the observation that the mantle contribution to melt progenitors of Macusani volcanics varied within a range of ~5 to 25 %, as suggested by Sr-Nd data, with most of the Lithium-rich Tuff data clustering in the higher mantle-contribution end (Fig. 10). Our models focus on the magma hybridization at or near the magma source region in the middle crust (Pichavant et al., 2024a). Since the bulk composition of ash-flow tuff samples may have been variably affected by the accumulation of crystal phases, the composition of the parental crystal mush can be tentatively calculated by inverting the evolution of the interstitial melts (Figs. S5 and S6). The degree of crystallization is tested at 20, 30, and 40%, i.e., lower than the 45-55 % crystal contents in Macusani Formation ash-flow tuff (Pichavant et al., 1988a; Cheilletz et al., 1992), for considering the crystal accumulation effect during the pyroclastic eruption and transport. This oversimplification does not consider the effect of antecrystal recycling in long-lived, large-volume, crystal-rich magmatic chambers (e.g., Jerram & Martin, 2008; Folkes et al., 2011). Assuming a 5% of mantle-derived component for ash-flow tuff parental melts, we added 20% of mantle-derived component in order to attain the 25 % suggested by Sr-Nd data for the Lithium-rich Tuff (Fig. 10).

Details on the calculation parameters and references are provided in Figures S5 and S6. This exercise allows us to critically evaluate if significant mantle contributions in felsic peraluminous magmas are compatible with the generation of highly evolved rare-metal-rich magmas.

To test the fit between the fractional crystallization models and the composition of Li-ore, we represented samples with LOI <2.7 wt %. The four models systematically underestimate the contents of elements that behaved as compatible (Sr, Ba, Ti, Pb; Fig. 12). While some models explain the contents of some elements that behaved as incompatible (Model 1: Be, W, Nb, and in part, Sn, Model 2: Sn, F; Model 3a: Be, Nb; Model 3b: Nb) and Nb/Ta ratios (Models 2 and 3b) in the Lithium-rich Tuff, some other incompatible elements are systematically underestimated (Li, Ta) or overestimated (Cs). Therefore, fractional crystallization alone does not provide a satisfactory explanation of the composition of the Lithium-rich Tuff, as a unique configuration is not consistently applicable to all elements (Figs. 11-12). Interestingly, Model 1 is insufficient to explain the enrichment in rare metals like Li, Sn, W, and Ta, W in the most evolved glass in ash-flow tuff (MH1 in Pichavant et al., 2024a) as well as a set of macusanite specimens (Fig. 11). This would agree with fractionation from non-cogenetic, spatially and/or temporally separate magma bodies as proposed by Pichavant et al. (1988a, b).

The models developed in this study suggest that the hybridization of magma with specialized (K-UK) mantle-derived melts does not result in a substantial depletion of the contents of Rb and Cs (Figs. 11 and S5). Conversely, it has been observed that this process can result in a differential increase in the contents of Li, Be, Sn, Nb, and Ta, which becomes progressively more pronounced through crystal fractionation. It is noteworthy that the high Sr, Ba, Ti, and Pb geochemical signature of mantle-derived magmas is largely cancelled out at fractional crystallization degrees higher than ~60 % (Fig. 12). This implies that the strong depletion in these elements in highly evolved, rare metal-rich felsic peraluminous magmas is not incompatible with a significant increase (20 %) in a mantle-derived component. It is also noteworthy that K-UK mafic series have been found to contain more than 0.4 wt % F (Edgar et al., 1996), which exceeds the ~0.25 wt % F on average calculated by Ballouard et al. (2023a) for anatectic melts in equilibrium with micas in suprasolidus metapelites, and the ~0.35 wt % F on average in suprasolidus orthogneiss. Consequently, even if the most significant source of F in Macusani magmas were micas from source metapelitic rocks (Pichavant et al., 1988b), a greater contribution of mantle-derived melts would enhance, rather than dilute, the F content in the magma source region. The elevated F concentrations in the peraluminous melt lowered the solidus and viscosity, delayed fluid-melt immiscibility (Troch et al., 2022), and facilitated shallower differentiation "*en route*" (Tartèse & Boulvais, 2010).

The underestimation of Li in all models is conspicuous and could be due to several reasons. Ballouard et al. (2023b) interpreted the substantial range of δ^7Li values and their positive correlation with Li contents in glass in ash-flow tuff from the Macusani Formation as a consequence of Li loss by equilibrium degassing or fluid exsolution of a Li-rich vapor/fluid from an initial rhyolitic melt with 750 ppm Li. This interpretation would involve that partition coefficients calculated by Pichavant et al. (2024a) for Li in Macusani volcanics may be overestimated and that the initial Li contents of the fractionating melts in our models are probably underestimated, resulting in the crystal fractionation models significantly underestimating the Li enrichment in the most evolved melts (Fig. 11). Furthermore, Pichavant et al. (1987) have invoked degassing of the magma prior to and during the eruption to explain the wide and negative range of δD values of macusanite. We hypothesize that, in addition to fractional crystallization, the exsolution of magmatic, ligand (e.g., F, B)-rich, volatile phases could have enhanced the enrichment of fluid-mobile elements such as Li and Ta (Brenan et al., 1998; London et al., 1988;

Thomas & Davidson, 2012; Iveson et al., 2019) in the magmas parental to the Li-ore. The involvement of these ligands has been deemed crucial to explain metal enrichment in rare-metal-rich, peraluminous granites and pegmatites (Ballouard et al., 2020; Troch et al., 2022).

The crystallization of Li-F micas from these highly evolved peraluminous melts, potentially in the presence of a magmatic-vapor phase, in the top layer of a crystal mush locked Li from a more severe depletion during degassing prior to and during eruption (cf. Neukampf et al., 2021, 2022). In this context, the explosive eruption was probably triggered by the progressive degassing from deeper, more fractionated, and compacted horizons of the magma reservoir, and upward migration and accumulation of a magmatic volatile phase (Cassidy et al., 2018; Townsend et al., 2019; Cortes-Calderon et al., in press).

Tephra segregation

The pronounced enrichment in elements that behaved as compatible, such as Sr, Ba, Pb, and Ti, in the Lithium-rich Tuff compared to crystal fractionation models and macusanite (Fig. 12) is inconsistent with the notion that its compositions can be explained exclusively in terms of strong differentiation of a rhyolitic melt. Instead, the systematic enrichment in these elements is consistent with the accumulation of feldspars and Li-F mica crystals (Fig. 12). To a certain extent, the accumulation of Li-F micas likely also contributed to the observed enrichment in Li relative to macusanite and the fractional crystallization models.

The physical accumulation of zircon and monazite would explain the higher zircon (T_{Zr}, based on Zr contents; Watson & Harrison, 1983) and monazite (T_{REE}, based on REE contents; Montel, 1993) saturation temperatures calculated for the Lithium-rich Tuff (650-720 °C; Fig. 13) compared to the main crystallization stage in Macusani magmas (~650 °C; Pichavant et al., 1988 a, b) and macusanite (T_{Zr} and T_{REE} of 600-700 °C, Fig. 13; liquidus temperature of 645 ± 10 °C at vapor saturation and 200 MPa according to experimental data of London et al., 1988).

Low-temperature, fluid-mediated processes

Secondary element mobility may certainly have occurred in the Li-ore units after their deposition. The pervasive alteration in Falchani is largely confined to the Upper and Lower Breccia, which strongly suggests that fluid-rock interaction at higher water/rock ratios was enhanced along the most permeable levels. In contrast, the Lithium-rich Tuff, which is characterized by a fine-grained and cohesive texture, was likely refractory to efficient circulation of surficial fluids. Notwithstanding the disparate degrees of alteration, the Lithium-rich Tuff and Upper and Lower Breccia record similar element mobility patterns in the isocon diagram (Fig. 6). The coupled depletion in alkalis (K_2O+Na_2O) and SiO_2, particularly in samples in which the alteration assemblages are dominated by smectite or zeolite (LOI = 8.2-13.5 wt %) as defined by Segovia-More et al. (2023), is consistent with alkali and silica leaching during feldspar and mica hydrolysis under alkaline pH conditions (Aagaard & Helgeson, 1983; Qinhua & Aizhen, 1991; Acker et al., 1992; Bagheri et al., 2022a, b; Jiménez et al., 2022).

Noteworthy, Cl and B were enriched in the most altered samples while F was depleted (Fig. 6). Alkaline, chloride-rich waters are common in geysers and cold springs in active geothermal systems along Neogene ignimbrite units in the region (e.g., El Tatio, in Chile, Cortecci et al., 2005) and could explain the enrichment in Cl in the most altered samples. The strong B metasomatism in Falchani might indicate participation of local groundwaters re-equilibrated with late Miocene ignimbrites and/or tourmaline-rich granites and metasedimentary rocks from the Paleozoic basement, similarly to what has been proposed for Cenozoic geothermal systems of the Argentina

Puna Plateau (Kasemann et al., 2004; Steinmetz et al., 2017). Regarding the distinctively high contents of Cs and Sr in zeolite-rich samples (e.g., 2021-MAC-053), these are consistent with Cs^+ and Sr^{2+} being selectively adsorbed onto zeolites such as mordenite (e.g., Munthali et al., 2015). Finally, it is also noteworthy that the post-depositional, low-T hydrothermal alteration at Falchani, particularly along the Upper and Lower Breccia, resulted in the partial leaching of Li (Fig. 6a). This is a notable contrast to other volcanogenic sedimentary deposits in which post-depositional processes are invoked to explain secondary lithium enrichment to economic grades, as discussed in the following section.

Volcanogenic sedimentary lithium deposits: Born or raised?

In volcanogenic sedimentary lithium deposits—a term used here broadly and interchangeably with volcano-sedimentary lithium deposits—lithium ore typically occurs in secondary minerals formed through *in situ* alteration of pre-enriched rhyolitic volcanic or volcanogenic sedimentary rocks (Starkey, 1982; Benson et al., 2017, 2023; Bowell et al., 2020; Borojević Šoštarić & Brenko, 2023). Regarding the role of pre-enriched protoliths in these deposits, Benson et al. (2017) demonstrated that rhyolitic rocks with higher proportions of felsic crustal contributions contain quartz-hosted glass inclusions enriched in Li. Our study confirms the dominant crustal component (>75%; Fig. 10) in the parental magma of the Li-ore units. However, both the proportion and nature of crustal components in magmas associated with the Li-ore units are comparable to those of other Neogene volcanogenic units in the Macusani Volcanic Field (e.g., Macusani Formation ash-flow tuff). This suggests that neither an increased proportion of crustal material nor a more felsic source rock alone can fully explain the elevated Li contents observed in the Li-ore units of the Macusani Volcanic Field.

Benson et al. (2023) proposed that peralkaline suites are most prospective for volcanogenic sedimentary lithium deposits due to their characteristically lower water contents and consequent reduced crystallization of Li-fractionating biotite. However, our findings from the Falchani deposit challenge this model, as they demonstrate an association with strongly peraluminous magmas. Indeed, the segregation of a magmatic-fluid phase in a shallow crustal magma reservoir could have enhanced primary enrichment of Li in Falchani. In this line of evidence, the occurrence of Li-F micas (zinnwaldite and lepidolite; Torró et al., 2023), typically associated with rare-metal granites and pegmatites, as crystal clasts in the Falchani Li ore (Fig. 3e) contrasts with other volcanogenic deposits and is probably fundamental to explain the distinctive primary (i.e., pre-eruptive) lithium enrichment in the studied tuffaceous rocks. We propose that Li was in part trapped in Li-F micas that crystallized at near-solidus temperatures (cf. Ellis et al., 2022) in the top layer of a crystal mush prior to explosive eruption. This mechanism would have minimized Li vapor loss and explains the exceptionally high lithium contents in the ejected pristine volcanic material (see also Cortes-Calderon et al., in press).

The formation of economic volcanogenic sedimentary lithium deposits typically requires lithium leaching and reconcentration in secondary minerals, particularly clays (Davis et al., 1986; Munk et al., 2011; Bowell et al., 2020; Benson et al., 2023). However, our results indicate that post-depositional, in situ alteration had minimal impact on lithium grades at Falchani. In fact, mass balance calculations reveal that post-eruptive alteration led to partial Li leaching, particularly along more permeable horizons (i.e., the Upper and Lower Breccia; Fig. 6).

To advance towards a metallogenic conceptualization for the Falchani deposit, an integrated perspective that incorporates crustal-scale magmatic evolution prior to the explosive eruption is necessary (Fig. 14). The correlation between felsic peraluminous magmatism and the thickest crust in the Andes (Ward et al., 2016) along the retroarc fold-thrust belt of the Eastern Cordillera (Perez et al., 2016) is conspicuous (Fig. 1). Crustal thickening through transcrustal ramp stacking after ca. 10 Ma (e.g., Garzione et al., 2017; Baby et al., 2018) likely promoted favorable conditions for partial melting of metasedimentary basement rocks (Wang et al., 2021) and extraction of magma batches from the source region (Rosenberg & Handy, 2005). Thermal priming of the crust in the Eastern Cordillera of southern Peru is evidenced by a significant influx of mantle-derived magmas and extensive crustal melting occurring during the Oligocene-Miocene (Sandeman et al., 1997; Carlier et al., 2005). During the late Miocene, the crust was thicker and hotter than in the late Oligocene (Garzione et al., 2017), which enhanced melting-assimilation-storage-homogenization (MASH) processes in a mid-crustal anatectic region (Pichavant et al., 2024a) and promoted the stability of long-lived magmatic reservoirs at shallower crustal depths (de Silva et al., 2006; Kaiser et al., 2017; de Silva & Kay, 2018). In this context, the T_{Zr} and T_{REE} calculated for the Lithium-rich Tuff parental magmas are lower than those of ash-flow tuff from the Macusani Formation and granites of the Quenamari Suite (Fig. 13), likely reflecting higher degrees of differentiation of a fluxing-rich magma (Pichavant et al., 2024a). These magmas reached saturation in zircon and monazite at or near the magma source region (see Montel, 1993), and then deviated from the T_{Zr}:T_{REE} 1:1 line through differentiation processes, following the evolution path of the macusanite glass (Fig. 13). The elevated F concentrations in the peraluminous melt lowered the solidus and viscosity, delayed fluid-melt immiscibility (Troch et al., 2022), and facilitated shallower differentiation *"en route"* (cf. Tartèse & Boulvais, 2010). Ongoing fractional crystallization probably led to magma degassing and possible migration of a magmatic-fluid phase through the crystal mush column (Ballouard et al., 2020; Troch et al., 2022; Tavazzani et al., 2024), which could have further enhanced the concentration in incompatible, fluid-mobile, lithophile elements in the top of the magma body. The crystallization of Li-F micas, either through direct magmatic crystallization or via melt-crystal-volatile interactions, prior to the explosive eruption likely sequestered a significant fraction of lithium, preventing its loss during syn-eruptive degassing. The subsequent incorporation of these Li-F-rich micas into the eruptive products resulted in the anomalously high lithium concentrations observed in the Li-ore at Falchani.

CONCLUSIONS

The composition of samples from Li-ore units of the Falchani Lithium Project in the Macusani Volcanic Field (i.e. Lithium-rich Tuff and Upper and Lower Breccia) indicates derivation from a strongly peraluminous and highly evolved rhyolitic magma with compositions that are equivalent to rare metal-rich peraluminous granites and LCT pegmatites. Their incompatible trace element compositions and REY patterns are more similar to those of macusanite than to previously reported ash-flow tuff from the Macusani Volcanic Field, which suggests derivation from highly evolved material, such as residual melts from the crystallization of the tuff parental magmas.

Mixing models based on Nd-Sr isotope ratios indicates a dominant contribution of Proterozoic and Paleozoic paragneiss and metapelite and <25 % of mantle contribution to the parental magma. The conspicuous felsic nature of the studied tuffaceous rocks could be explained in part by the high crustal contribution compared to other late Miocene ignimbrite fields in the Neogene Ignimbrite Province of the Central Andes.

Fractional crystallization was the most important mechanism for the rare metal enrichment in Macusani melts, but it is insufficient to fully account for the composition of the volcanogenic Li ore. Pre-eruptive metasomatism involving a magmatic volatile phase exsolved from a volatile-rich, highly fractionated, crystal-rich magmatic reservoir could have increased the concentration of fluid-mobile elements such as Li in the top of a mushy magma body. In addition, the accumulation of crystals, including plagioclase and Li-F micas, during tephra transport explains the observed enrichment in elements that behaved as compatible.

In contrast to most volcanogenic sedimentary lithium deposits, the pre-eruptive magmatic evolution was the key to upgrading Li contents to economic levels in Li-ore units at Falchani, while post-eruptive, in situ alteration processes associated with the formation of secondary clays and zeolites promoted Li leaching, but not enrichment. We attribute this feature to the extreme magma differentiation favored by elevated F concentrations that lowered the solidus and the possible segregation of a magmatic-vapor phase strongly enriched in incompatible volatile elements in a mushy magma body leading to the crystallization of lithium minerals such as zinnwaldite and lepidolite micas, previous to the eventual eruption.

FUNDING

This work was supported by the Peruvian project 122-2020 E041-2020-01-01 managed through the PROCIENCIA agency.

ACKNOWLEDGEMENTS

We thank Macusani Yellowcake S.A.C., especially Dr. Ulises Solís and Eng. Gregorio Tasayco, for facilitating access to drill cores, and geologists Miguel Cavani, Roher Huaricallo, and Henry Mamani for their invaluable insights and discussions on the geology of the Macusani volcanic field. We are also grateful to Mathieu Benoit for his help with TIMS data acquisition and discussion, and to Mariana Segovia-More, Joaquín A. Proenza, Cristina Villanova-de-Benavent, Loïs Monnier, and Stefano Salvi for their contributions to the discussion of the mineralogy of the ore units. The detailed and constructive comments of Michel Pichavant, Julie Michaud, and Francesco Putzolu and the efficient editorial handling by Associate Editor Valentin Troll and Editor-in-Chief Georg Zellmer are greatly appreciated.

SUPPLEMENTARY DATA

Supplementary data are available at Journal of Petrology online.

DATA AVAILABILITY

The data presented in this article are available in the online supplemental materials.

REFERENCES

Aagaard, P. & Helgeson, H. C. (1983). Activity/composition relations among silicates and aqueous solutions: II. Chemical and thermodynamic consequences of ideal mixing of atoms on homological sites in montmorillonites, illites, and mixed-layer clays. *Clays and Clay Minerals* 31, 207-217. https://doi.org/10.1346/CCMN.1983.0310306.

Acker, J. G. & Bricker, O. P. (1992). The influence of pH on biotite dissolution and alteration kinetics at low temperature. *Geochimica et Cosmochimica Acta* 56, 3073−3092. https://doi.org/10.1016/0016-7037(92)90290-Y.

Allmendinger, R. W., Jordan, T. E., Kay, S. M. & Isacks, B. L. (1997). The evolution of the Altiplano-Puna plateau of the Central Andes. *Annual Review of Earth and Planetary Sciences* 25, 139–74.

Armijo, R., Lacassin, R., Coudurier-Curveur, A. & Carrizo, D. (2015). Coupled tectonic evolution of Andean orogeny and global climate. *Earth-Science Reviews* 143, 1-35. https://doi.org/10.1016/j.earscirev.2015.01.005.

Arribas, A. & Figueroa, E. (1985). Las mineralizaciones de uranio en las rocas volcánicas de Macusani, Puno (Perú). *Estudios Geológicos* 41, 323–342. https://doi.org/10.3989/egeol.85415-6714.

Audebaud, E. (1973). Geología de los cuadrángulos de Ocongate y Sicuani. Instituto Geológico Minero y Metalúrgico, Boletín 25, 72 pp.

Baby, P., Calderón, Y., Hurtado, C., Louterbach, M., Espurt, N., Brusset, S., Roddaz, M., Brichau, S., Eude, A. & Calvès, G. (2018). *The Peruvian sub-andean foreland basin system: Structural overview, geochronologic constraints, and unexplored plays*. In: Zamora, G., McClay, K. R. & Ramos, V. A. (eds.) *Petroleum Basins and Hydrocarbon Potential of the Andes of Peru and Bolivia*. AAPG Special Volumes 117, 87–116. https://doi.org/10.1306/13622118M1173767.

Bagheri, M., Lothenbach, B., Shakoorioskooie, M. & Scrivener, K. (2022a). Effect of different ions on dissolution rates of silica and feldspars at high pH. *Cement and Concrete Research* 152, 106644. https://doi.org/10.1016/j.cemconres.2021.106644.

Bagheri, M., Lothenbach, B., Shakoorioskooie, M. & Scrivener, K. (2022b). Corrigendum to "Effect of different ions on dissolution rates of silica and feldspars at high pH". *Cement and Concrete Research* 160:106928. https://doi.org/10.1016/j.cemconres.2022.106928

Baker, M. C. W. (1981). The nature and distribution of upper Cenozoic ignimbrite centres in the Central Andes. *Journal of Volcanology and Geothermal Research* 11, 29–315. https://doi.org/10.1016/0377-0273(81)90028-7.

Ballouard, C., Poujol, M., Boulvais, P., Branquet, Y., Tartèse, R. & Vigneresse, J. L. (2016). Nb-Ta fractionation in peraluminous granites: A marker of the magmatic-hydrothermal transition. *Geology* 44, 231–234. https://doi.org/10.1130/G37475.1.

Ballouard, C., Massuyeau, M., Elburg, M., Tappe, S., Viljoen, F. & Brandenburg, J.-T. (2020). The magmatic and magmatic-hydrothermal evolution of felsic igneous rocks as seen through Nb-Ta geochemical fractionation, with implications for the origins of rare-metal mineralizations. *Earth-Science Reviews* 203, 103115. https://doi.org/10.1016/j.earscirev.2020.103115.

Ballouard, C., Couzinié, S., Bouilhol, P., Harlaux, M., Mercadier, J. & Montel, J.-M. (2023a). A felsic meta-igneous source for Li-F-rich peraluminous granites: insights from the Variscan

Velay dome (French Massif Central) and implications for rare-metal magmatism. *Contributions to Mineralogy and Petrology* 178, 75. https://doi.org/10.1007/s00410-023-02057-1.

Ballouard, C., Marrocchi, Y., Millot, R., Mercadier, J., Bouden, N., Lach, P., Eglinger, A., Laurent, O., Jérémie, M., Elburg, M. & Pichavant, M. (2023b). *L'isotopie du Li dans les micas par microsonde ionique: développement et applications aux Tufs volcaniques de Macusani (Pérou) et aux pegmatites à métaux rares de la ceinture de la Rivière Orange du Namaqualand (Afrique du Sud)* [Conference presentation] 28ème Edition de la Réunion des Sciences de la Terre, Rennes, France.

Barnes, V. E., Edwards, G., McLaughlin, W. A., Friedman, I. & Joensuu, O. (1970). Macusanite occurrence, age, and composition, Macusani, Peru. *Geological Society of America Bulletin* 81, 1539–1546, https://doi.org/10.1130/0016-7606(1970)81[1539:MOAACM]2.0.CO;2.

Bau, M. (1996). Controls on the fractionation of isovalent trace elements in magmatic and aqueous systems: Evidence from Y/Ho, Zr/Hf and lanthanide tetrad effect. *Contributions to Mineralogy and Petrology* 123, 323-333. https://doi.org/10.1007/s004100050159.

Benjamin, M. T., Johnson, N. M. & Naeser, C. W. (1987). Recent rapid uplift in the Bolivian Andes: Evidence from fission-track dating. *Geology* 15, 680–83. https://doi.org/10.1130/0091-7613(1987)15<680:RRUITB>2.0.CO;2.

Benson, T. R., Coble, M. A., Rytuba, J. J. & Mahood, G. A. (2017). Lithium enrichment in intracontinental rhyolite magmas leads to Li deposits in caldera basins. *Nature Communications* 8, 270. https://doi.org/10.1038/s41467-017-00234-y.

Benson, T. R., Coble, M. A. & Dilles, J. H. (2023). Hydrothermal enrichment of lithium in intracaldera illite-bearing claystones. *Science Advances* 9, 8183. https://doi.org/10.1126/sciadv.adh8183.

Borojević, S. & Brenko, T. (2022). The Miocene Western Balkan lithium-boron metallogenic zone. *Mineralium Deposita* 58, 639–658. https://doi.org/10.1007/s00126-022-01151-x.

Bowell, R. J., Lagos, L., de los Hoyos, C. R. & Declercq, J. (2020). Classification and characteristics of natural lithium resources. *Elements* 16, 259–264. https://doi.org/10.2138/gselements.16.4.259.

Brenan, J. M., Ryerson, F. J. & Shaw, H. F. (1998). The role of aqueous fluids in the slab-to-mantle transfer of boron, beryllium, and lithium during subduction: Experiments and models. *Geochimica et Cosmochimica Acta* 62, 3337–3347. https://doi.org/10.1016/S0016-7037(98)00224-5.

Buford Parks, V., McQuarrie, N., Falkowski, S., Perez, N. & Ehlers, T. (2023). Timing and drivers of exhumation and sedimentation in the eastern Peruvian Andes: Insights from thermokinematic modelling. *Earth and Planetary Science Letters* 620, 118355. https://doi.org/10.1016/j.epsl.2023.118355.

Carlier, G., Lorand, J. P., Liégeois, J. P., Fornari, M., Soler, P., Carlotto, V. & Cardenas, J. (2005). Potassic-ultrapotassic mafic rocks delineate two lithospheric mantle blocks beneath the southern Peruvian Altiplano. *Geology* 33, 601–604. https://doi.org/10.1130/G21643.1.

Carlotto, V., Carlier, G., Van Heiningen, P., Blake Hodgin, E., Cárdenas, J., Ligarda, R., Cerpa, L. & Maqquera, V. (2023). Andean evolution, orogenic deformation and uplift of the Western Cordillera and Altiplano of southern Peru, northern Bolivia and Chile: Eocene-Oligocene lithospheric delamination. *Journal of South American Earth Sciences* 128, 104423. https://doi.org/10.1016/j.jsames.2023.104423.

Cas, R. F. & Wright, J. V. (1988). *Volcanic Successions Modern and Ancient*. Springer. https://doi.org/10.1007/978-94-009-3167-1.

Cassidy, M., Manga, M., Cashman, K. & Bachmann, O. (2018). Controls on explosive-effusive volcanic eruption styles. *Nature Communications* 9, 2839. https://doi.org/10.1038/s41467-018-05293-3

Cheilletz, A., Clark, A. H., Farrar, E., Arroyo Pauca, G., Pichavant, M. & Sandeman, H. A. (1992). Volcano-stratigraphy and ^{40}Ar/^{39}Ar geochronology of the Macusani ignimbrite field: monitor of the Miocene geodynamic evolution of the Andes of southeast Peru. *Tectonophysics* 205, 307–327. https://doi.org/10.1016/0040-1951(92)90433-7.

Chew, D. M., Pedemonte, G. & Corbett, E. (2016). Proto-Andean evolution of the Eastern Cordillera of Peru. *Gondwana Research* 35, 59-78. https://doi.org/10.1016/j.gr.2016.03.016.

Chiaradia, M., Müntener, O. & Beate, B. (2020). Effects of aseismic ridge subduction on the geochemistry of frontal arc magmas. *Earth and Planetary Science Letters* 531, 115984. https://doi.org/10.1016/j.epsl.2019.115984.

Choquehuanca, S., Latorre, O. & Soberon, D. (2015). Mapa geológico del cuadrángulo de Corani - Hoja 28u3 Carta Geológica Nacional Digital Escala 1: 50 000: Instituto Geológico Minero y Metalúrgico, scale 1:50,000.

Clark, A. H., Palma, V. V., Archibald, D. A., Farrar, E., Mario, J., Arenas, F. & Robertson, R. C. (1983). Occurrence and age of tin mineralization in the Cordillera Oriental, Southern Peru. *Economic Geology* 78:514–520. https://doi.org/10.2113/gsecongeo.78.3.514.

Clark, A., Farrar, E., Kontak, D., Langridge, R., Arenas, M., France, L., McBride, S., Woodman, H., Wasteneys, H., Sandeman, H. & Archibald, D. (1990). Geologic and geochronologic constraints on the metallogenic evolution of the Andes of southeastern Peru. *Economic Geology* 85:1520-1583. https://doi.org/10.2113/gsecongeo.85.7.1520.

Clarke, S. (2023). American Lithium Announces 476% Increase in Measured + Indicated Lithium Resources at Falchani – Adds K, Cs and Rb to Block Model. https://americanlithiumcorp.com/american-lithium-announces-476-increase-in-measured-indicated-lithium-resources-at-falchani-adds-k-cs-and-rb-to-block-model (accessed 10 December 2023).

Cortecci, G., Boschetti, T., Mussi, M., Herrera, C., Mucchino, C. & Barbieri, M. (2005). New chemical and original isotopic data on waters from El Tatio geothermal field, northern Chile. *Geochemical Journal* 39, 547-571. https://doi.org/10.2343/geochemj.39.547.

Cortes-Calderon, E. A., Ellis, B. S., Tavazzani, L., Magna, T., Harris, C. & Benson, T. R. (in press). Lithium inventory of the Cerro Galán volcanic system (Argentina): The role of magmatism as source for Li-bearing brine. *Economic Geology*.

Couzinié, S., Laurent, O., Chelle-Michou, C., Bouilhol, P., Paquette, J.-L., Gannoun, A.-M. & Moyen, J.-F. (2019). Detrital zircon U–Pb–Hf systematics of Ediacaran metasediments from the French Massif Central: Consequences for the crustal evolution of the north Gondwana margin. *Precambrian Research* 324, 269-284. https://doi.org/10.1016/j.precamres.2019.01.016.

Craig, N., Speakman, R. J., Popelka-Filcoff, R. S., Aldenderfer, M., Flores Blanco, L., Vega, M. B. & Stanish, C. (2010). Macusani obsidian from southern Peru: A characterization of its elemental composition with a demonstration of its ancient use. *Journal of Archaeological Science* 37, 569–576. https://doi.org/10.1016/j.jas.2009.10.021.

Davis, J., Friedman, I. & Gleason, D. (1986). Origin of the lithium-rich brine, Clayton Valley, Nevada. U.S. Geological Survey Bulletin 1622. Shorter contributions to isotope research, Chaper L.

Debon, F. & Le Fort, P. (1983). A chemical-mineralogical classification of common plutonic rocks and associations. *Earth and Environmental Science Transactions of The Royal Society of Edinburgh* 73, 135-149. https://doi.org/10.1017/S0263593300010117.

DePaolo, D. J. (1981). A neodymium and strontium isotopic study of the Mesozoic calc-alkaline granitic batholiths of the Sierra Nevada and Peninsular Ranges, California. *Journal of Geophysical Research: Solid Earth* 86, 10470-10488. https://doi.org/10.1029/JB086iB11p10470.

de Silva, S. L. (1989a). The Altiplano–Puna Volcanic Complex of the Central Andes. *Geology* 17, 1102–1106. https://doi.org/10.1130/0091-7613(1989)017<1102:APVCOT>2.3.CO;2.

de Silva, S. L. (1989b). Geochronology and stratigraphy of the ignimbrites from the 21°30'S to 23°30'S portion of the Central Andes of northern Chile. *Journal of Volcanology and Geothermal Research* 37, 93–131. https://doi.org/10.1016/0377-0273(89)90065-6.

de Silva, S. L. & Gosnold, W. D. (2007). Episodic construction of batholiths: Insights from the spatiotemporal development of an ignimbrite flare-up. *Journal of Volcanology and Geothermal Research* 167, 320–335. https://doi.org/10.1016/j.jvolgeores.2007.07.015.

de Silva, S. L. & Kay, S. M. (2018). Turning up the heat: high-flux magmatism in the Central Andes. *Elements* 14, 245-250. https://doi.org/10.2138/gselements.14.4.245.

de Silva, S. L., Zandt, G., Trumbull, R., Viramonte, J., Salas, G. & Jiménez, N. (2006). Large ignimbrite eruptions and volcanotectonic depressions in the Central Andes: A thermomechanical perspective. In: de Natale, G., Troise, C. & Kilburn, C. (eds.) *Mechanisms of Activity and Unrests at Large Calderas*. Geological Society Special Publication 269, 47–63.

DIGIS Team (2023). GEOROC Compilation Convergent Margins. https://doi.org/10.25625/PVFZCE

Dorbath, C., Granet, M., Poupinet, G. & Martinez, C. (1993). A teleseismic study of the Altiplano and the Eastern Cordillera in northern Bolivia: New constraints on a lithospheric model. *Journal of Geophysical Research: Solid Earth* 98, 9825–9844. https://doi.org/10.1029/92JB02406.

Edgar, A. D., Pizzolato, L. A. & Sheen, J. (1996). Fluorine in igneous rocks and minerals with emphasis on ultrapotassic mafic and ultramafic magmas and their mantle source regions. *Mineralogical Magazine* 60, 243-257. https://doi.org/10.1180/minmag.1996.060.399.01.

Ellis, B. S., Neukampf, J., Bachmann, O., Harris, C., Forni, F., Magna, T., Laurent, O. & Ulmer, P. (2022). Biotite as a recorder of an exsolved Li-rich volatile phase in upper-crustal silicic magma reservoirs. *Geology* 50, 481–485. https://doi.org/10.1130/G49484.1.

Elliott, J. & Moss, A. (1965). Natural glass from Macusani, Peru. *Mineralogical Magazine* 35, 423–424. https://doi.org/10.1180/minmag.1965.035.270.18.

Farina, F., Dini, A., Rocchi, S. & Stevens, G. (2014). Extreme mineral-scale Sr isotope heterogeneity in granites by disequilibrium melting of the crust. *Earth and Planetary Science Letters* 399, 103–115. https://doi.org/10.1016/j.epsl.2014.05.018.

Farrar, E., Clark, A. H., Kontak, D. J., Archibald, D. A. (1988). Zongo-San Gaban zone: Eocene foreland boundary of the Central Andean orogen, northwest Bolivia and southeast Peru. *Geology* 16, 55-58. https://doi.org/10.1130/0091-7613(1988)016<0055:ZSGNZE>2.3.CO;2.

Faure, G. & Mensing, T. M. (2005). *Isotopes: principles and applications*, 3rd edn. Wiley & Sons, Hoboken, 873 pp.

Folkes, C. B., de Silva, S., Schmitt, A. K. & Cas, R. A. F. (2011). A reconnaissance of U-Pb zircon ages in the Cerro Galán system, NW Argentina: prolonged magma residence, crystal recycling, and crustal assimilation. *Journal of Volcanology and Geothermal Research* 206, 136–147. https://doi.org/10.1016/j.jvolgeores.2011.06.001.

Francis, G. H. (1959). Ignimbritas (sillar) de la Cordillera Oriental del sur del Perú. *Instituto Nacional de Investigaciones y Fomento Minero, Boletín* 21, 13-32.

French, B. M. & Meyer, H. O. A. (1970). *Andalusite and " β-quartz" in Macusani glass, Peru.* Carnegie Institute Washington, Year Book 68, 339-342.

French, B. M., Jezek, P. A. & Appleman, D. E. (1978). Virgilite: A new lithium aluminum silicate mineral from the Macusani glass, Peru. *American Mineralogist* 63, 461–465.

Garcia, D., Fonteilles, M. & Moutte, J. (1994). Sedimentary fractionations between Al, Ti, and Zr and the genesis of strongly peraluminous granites. *The Journal of Geology* 102, 411–422. https://doi.org/10.1086/629683.

Gardeweg, P. M. & Ramirez, C. F. (1987). The La Pacana Caldera and the Atana ignimbrite: A major ash-flow and resurgent caldera complex in the Andes of northern Chile. *Bulletin of Volcanology* 49, 547-566. https://doi.org/10.1007/BF01080449.

Garzione, C. N., McQuarrie, N., Perez, N., Ehlers, T., Beck, S., Kar, N., Eichelberger, N., Chapman, A., Ward, K., Ducea, M., Lease, R., Poulsen, C., Wagner, L., Saylor, J., Zandt, G. & Horton, B. (2017). Tectonic evolution of the central Andean plateau and implications for the growth of plateaus. *Annual Review of Earth and Planetary Sciences* 45, 529–559. https://doi.org/10.1146/annurev-earth-063016-020612.

Gérard, B., Robert, X., Audin, L., Valla, P. G., Bernet, M. & Gautheron, C. (2021). Differential exhumation of the Eastern Cordillera in the Central Andes: Evidence for south-verging backthrusting (Abancay Deflection, Peru). *Tectonics* 40, e2020TC006314. https://doi.org/10.1029/2020TC006314.

Gillis, R., Horton, B. & Grove, M. (2006). Thermochronology, geochronology, and upper crustal structure of the Cordillera Real: Implications for Cenozoic exhumation of the central Andean plateau. *Tectonics* 25, TC6007. https://doi.org/10.1029/2005TC001887.

Goldstein, S. L., O'Nions, R. K. & Hamilton, P. J. (1984). A Sm-Nd study of atmospheric dusts and particulates from major river systems. *Earth and Planetary Science Letters* 70, 221-236. https://doi.org/10.1016/0012-821X(84)90007-4.

Grant, J. A. (1986). The isocon diagram—a simple solution to Gresens' equation for metasomatic alteration. *Economic Geology* 81, 1976–1982. https://doi.org/10.2113/gsecongeo.81.8.1976.

Grant, J. A. (2005). Isocon analysis: a brief review of the method and applications. *Physics and Chemistry of the Earth*, 30, 997-1004. https://doi.org/10.1016/j.pce.2004.11.003.

Guillong, M., Meier, D. L., Allan, M. M., Heinrich, C. A. & Yardley, B. W. (2008). Appendix A6: SILLS: A MATLAB-based program for the reduction of laser ablation ICP-MS data of homogeneous materials and inclusions. *Mineralogical Association of Canada Short Course* 40, 328–333.

Guillot, S. & Le Fort, P. (1995). Geochemical constraints on the bimodal origin of High Himalayan leucogranites. *Lithos* 35, 221–234. https://doi.org/10.1016/0024-4937(94)00052-4.

Harlaux, M., Kouzmanov, K., Gialli, S., Clark, A. H., Laurent, O., Corthay, G., Prado Flores, E., Dini, A., Chauvet, A., Ulianov, A., Chiaradia, M., Menzies, A., Villón Durand, G., Kalinaj, M. & Fontboté, L. (2021). The Upper Oligocene San Rafael intrusive complex (Eastern Cordillera, southeast Peru), host of the largest-known high-grade tin deposit. *Lithos* 400-401, 106409. https://doi.org/10.1016/j.lithos.2021.106409.

Heinonen, J., Iles, K., Heinonen, A., Fred, R., Virtanen, V., Bohrson, W. & Spera, F. (2021). From binary mixing to magma chamber simulator - Geochemical modeling of assimilation in magmatic systems. In: Masotta, M., Beier, C. & Mollo, S. (eds.) *Crustal Magmatic System Evolution: Anatomy, Architecture, and Physico‐Chemical Processes*. Geophysical Monograph Series, American Geophysical Union, 151-176. https://doi.org/10.1002/9781119564485.ch7.

Hill, I. G., Worden, R. H., & Meighan, I. G. (2000). Yttrium: the immobility-mobility transition during basaltic weathering. *Geology* 28, 923–926. https://doi.org/10.1130/0091-7613(2000)28<923:YTITDB>2.0.CO;2.

Horton, B. K. (2018). Tectonic regimes of the central and southern Andes: Responses to variations in plate coupling during subduction. *Tectonics* 37, 402–429. https://doi.org/10.1002/2017TC004624.

Iveson, A. A., Webster, J. D., Rowe, M. C. & Neill, O. K. (2019). Fluid-melt trace-element partitioning behaviour between evolved melts and aqueous fluids: Experimental constraints on the magmatic-hydrothermal transport of metals. *Chemical Geology* 516:18–41. https://doi.org/10.1016/j.chemgeo.2019.03.029.

Jerram, D. A. & Martin, V. M. (2008). Understanding crystal populations and their significance through the magma plumbing system. In: C. Annen & G. F. Zellmer (Eds.), *Dynamics of Crustal Magma Transfer, Storage and Differentiation*. *Geological Society, London, Special Publications* 304, 133–148. https://doi.org/10.1144/SP304.7.

Jiménez, J., Gimeno, M. & Auqué, F. (2022). Geochemical characterisation and modelling of the Luchon hydrothermal system (Central Pyrenees, France) and lessons learnt for the use of geochemical modelling techniques in granite-hosted alkaline thermal waters. *Geothermics* 106, 102573. https://doi.org/10.1016/j.geothermics.2022.102573.

Jochum, K. P., Weis, U., Stoll, B., Kuzmin, D., Yang, Q., Raczek, I., Jacob, D. E., Stracke, A., Birbaum, K., Frick, D. A., Günther, D. & Enzweiler, J. (2011). Determination of reference values for NIST SRM 610-617 glasses following ISO guidelines. *Geostandards and Geoanalytical Research* 35, 397–429. https://doi.org/10.1111/j.1751-908X.2011.00120.x.

Kaiser, J. F., de Silva, S., Schmitt, A. K., Economos, R. & Sunagua, M. (2017). Million-year melt–presence in monotonous intermediate magma for a volcanic–plutonic assemblage in the Central Andes: Contrasting histories of crystal-rich and crystal-poor super-sized silicic magmas. *Earth and Planetary Science Letters* 457, 73–86. https://doi.org/10.1016/j.epsl.2016.09.048.

Kasemann, S. A., Meixner, A., Erzinger, J., Viramonte, J. G., Alonso, R. N. & Franz, G. (2004). Boron isotope composition of geothermal fluids and borate minerals from salar deposits (central Andes/NW Argentina). *Journal of South American Earth Sciences* 16, 685–697. https://doi.org/10.1016/j.jsames.2003.12.004.

Kato, J. J. (2013). Geochemistry of the Neogene Los Frailes Ignimbrite Complex on the Central Andean Altiplano plateau. Master dissertation, Cornell University.

Kay, S. M., Coira, B. L., Caffe, P. J. & Chen, C.-H. (2010). Regional chemical diversity, crustal and mantle sources and evolution of central Andean Puna plateau ignimbrites. *Journal of Volcanology and Geothermal Research* 198, 81-111. https://doi.org/10.1016/j.jvolgeores.2010.08.013.

Kley, J., Müller, J., Tawackoli, S., Jacobshagen, V. & Manutsoglu, E. (1997). Pre-Andean and Andean-age deformation in the Eastern Cordillera of southern Bolivia. *Journal of South American Earth Sciences* 10, 1–19. https://doi.org/10.1016/S0895-9811(97)00001-1.

Kontak, D. J., Clark, A. H., Farrar, E., Archibald, D. A. & Baadsgaard, H. (1990). Late Paleozoic-early Mesozoic magmatism in the Cordillera de Carabaya, Puno, southeastern Peru: Geochronology and petrochemistry. *Journal of South American Earth Sciences* 3, 213–230. https://doi.org/10.1016/0895-9811(90)90004-K.

Labou, I., Benoit, M., Baratoux, L., Grégoire, M., Ndiaye, P.M., Thebaud, N., Béziat, D. & Debat, P. (2020). Petrological and geochemical study of Birimian ultramafic rocks within the West African Craton: Insights from Mako (Senegal) and Loraboué (Burkina Faso) lherzolite/harzburgite/wehrlite associations. *Journal of African Earth Sciences* 162, 103677. https://doi.org/10.1016/j.jafrearsci.2019.103677.

Laubacher, G. (1978). Estudio geológico de la región norte del lago Titicaca. Instituto Geológico, Minero y Metalúrgico, 120 pp.

Le Maitre, R. W., Bateman, P., Dudek, A., Keller, J., Lameyre, J., Le Bas, M. J., Sabine, P. A., Schmid, R., Sorensen, H., Streckeisen, A., Woolley, A. R. & Zanettin, B. (1989). A classification of igneous rocks and glossary of terms: Recommendations of the International Union of Geological Sciences Subcommission on the Systematics of Igneous Rocks. Blackwell Scientific Publications, Oxford, U.K.

Li, V. (2016). The Uranium Mineralization of the Macusani District, southeast Peru: Mineralogy, Geochemistry, Geochronology and Ore-genetic Model. Doctoral dissertation, Kingston, ON, Queen’s University

Li, C. F., Li, X., Li, Q., Guo, J. & Li, X. (2011). Directly determining ^{143}Nd/^{144}Nd isotope ratios using thermal ionization mass spectrometry for geological samples without separation of Sm-Nd. *Journal of Analytical Atomic Spectrometry* 26, 2012-2022. https://doi.org/10.1039/C0JA00081G.

Li, C.-F., Li, X.-H., Li, Q.-L., Guo, J.-H., Li, X.-H. & Yang, Y.-H. (2012). Rapid and precise determination of Sr and Nd isotopic ratios in geological samples from the same filament loading by thermal ionization mass spectrometry employing a single-step separation scheme. *Analytica Chimica Acta* 727, 54-60. https://doi.org/10.1016/j.aca.2012.03.040.

Linck, G. (1926). Ein neuer knstallfiihrender Tektit von Paucartambo in Peru. *Chemie der Erde* 2, 57-174.

Lindsay, J. M., Schmitt, A. K., Trumbull, R. B., de Silva, S. L., Siebel, W. & Emmermann, R. (2001). Magmatic evolution of the La Pacana Caldera System, Central Andes, Chile: Compositional variation of two cogenetic, large-volume felsic ignimbrites. *Journal of Petrology* 42, 459–486. https://doi.org/10.1093/petrology/42.3.459.

Linnen, R. L. & Keppler, H. (1997). Columbite solubility in granitic melts: consequences for the enrichment and fractionation of Nb and Ta in the Earth's crust. *Contributions to Mineralogy and Petrology* 128, 213–227. https://doi.org/10.1007/s004100050304.

Linnen, R. L. & Keppler, H. (2002). Melt composition control of Zr/Hf fractionation in magmatic processes. *Geochimica et Cosmochimica Acta* 66, 3293–3301. https://doi.org/10.1016/S0016-7037(02)00924-9.

Loewy, S., Connelly, J. & Dalziel, I. (2004). An orphaned basement block: The Arequipa-Antofalla Basement of the central Andean margin of South America. Geological *Society of America Bulletin* 116, 171-187. https://doi.org/10.1130/B25226.1.

London, D., Hervig, R. L. & Morgan, G. B. (1988). Melt-vapor solubilities and elemental partitioning in peraluminous granite-pegmatite systems: Experimental results with Macusani glass at 200 MPa. *Contributions to Mineralogy and Petrology* 99, 360–373. https://doi.org/10.1007/BF00375368.

López, J. C. (1996). Geología del cuadrángulo de Nuñoa. Hoja 29-u. Instituto Geológico, Minero y Metalúrgico, 171pp.

López Steinmetz, R. L. & Salvi, S. (2021). Brine grades in Andean salars: When basin size matters. A review of the Lithium Triangle. *Earth-Science Reviews* 217, 103615. https://doi.org/10.1016/j.earscirev.2021.103615.

Lugmair, G. W. & Marti, K. (1978). Lunar initial ^{143}Nd/^{144}Nd: differential evolution of the lunar crust and mantle. *Earth and Planetary Science Letters* 39, 349-357. https://doi.org/10.1016/0012-821X(78)90021-3.

MacDonald, R., Smith, R. L. & Thomas, J. E. (1992). Chemistry of the subalkalic silicic obsidians. U.S. Geological Survey Professional Paper 1523, 214 pp.

Martin, R. & de Sitter-Koomans, C. (1955). Pseudotectites from Colombia and Peru. *Leidse Geologische Mededelingen* 20, 151–164.

Martínez, A., Clausen, N., Memeti, V. & Paterson, S. (2019). Source contamination, crustal assimilation, and magmatic recycling during three flare-up events in the Cretaceous Peruvian Coastal Batholith: An example from the Ica-Pisco plutons. *Journal of South American Earth Sciences* 95, 102300. https://doi.org/10.1016/j.jsames.2019.102300.

McCulloch, M. T., Jaques, A. L., Nelson, D. R., & Lewis, J. D. (1983). Nd and Sr isotopes in kimberlites and lamproites from western Australia: An enriched mantle origin. *Nature* 302, 400–403. https://doi.org/10.1038/302400a0.

McDonough, W. F. & Sun, S. S. (1995). Composition of the Earth. *Chemical Geology* 120, 223-253. https://doi.org/10.1016/0009-2541(94)00140-4.

McPhie, J., Doyle, M. & Allen, R. (1993). *Volcanic textures: a guide to the interpretation of textures in volcanic rocks*. Centre for Ore Deposit and Exploration Studies, University of Tasmania.

Mégard, F. (1978). Etude géologique des Andes du Pérou central. ORSTOM, Paris, 310 pp.

Meixner, A., Sarchi, C., Lucassen, F., Becchio, R., Caffe, P. J., Lindsay, J., Rosner, M. & Kasemann, S. A. (2020). Lithium concentrations and isotope signatures of Palaeozoic basement rocks and Cenozoic volcanic rocks from the Central Andean arc and back-arc. *Mineralium Deposita* 55, 1071–1084. https://doi.org/10.1007/s00126-019-00915-2.

Michard, A., Gurriet, P., Soudant, M. & Albarede, F. (1985). Nd isotopes in French phanerozoic shales: External vs internal aspects of crustal evolution. *Geochimica et Cosmochimica Acta* 49, 601–610. https://doi.org/10.1016/0016-7037(85)90051-1.

Michaud, J., Pichavant, M. & Villaros, A. (2021). Rare elements enrichment in crustal peraluminous magmas: Insights from partial melting experiments. *Contributions to Mineralogy and Petrology* 176, 33. https://doi.org/10.1007/s00410-021-01855-9.. .insu-03431952.

Mišković, A., Spikings, R. A., Chew, D. M., Košler, J., Ulianov, A. & Schaltegger, U. (2009). Tectonomagmatic evolution of Western Amazonia: Geochemical characterization and zircon U-Pb geochronologic constraints from the Peruvian Eastern Cordilleran granitoids. *Geological Society of America Bulletin* 121, 1298–1324. https://doi.org/10.1130/B26488.1.

Montel, J.-M. (1993). A model for monazite/melt equilibrium and application to the generation of granitic magmas. *Chemical Geology* 110, 127–146. https://doi.org/10.1016/0009-2541(93)90250-M.

Munk, L. A., Jochens, H., Jennings, M., Bradley, D., Hynek, S. & Godfrey, L. (2011). Geochemistry of lithium-rich brines in Clayton Valley, Nevada, USA. 11th SGA Biennial Meeting Let's Talk Ore Deposits 26-29th September 2011 Antofagasta, Chile, 217-219.

Munthali, N. W., Johan, E., Aono, H. & Matsue, N. (2015). Cs^+ and Sr^{2+} adsorption selectivity of zeolites in relation to radioactive decontamination. *Journal of Asian Ceramic Society* 3, 245–250. https://doi.org/10.1016/j.jascer.2015.04.002.

Neukampf, J., Ellis, B. S., Laurent, O., Steinmann, L. K., Ubide, T., Oeser, M., Magna, T., Weyer, S. & Bachmann, O. (2021). Time scales of syn-eruptive volatile loss in silicic magmas quantified by Li-isotopes. *Geology* 49, 125–129. https://doi.org/10.1130/G47764.1.

Neukampf, J., Laurent, O., Tollan, P., Bouvier, A.-S., Magna, T., Ulmer, P., France, L., Ellis, B. S. & Bachmann, O. (2022). Degassing from magma reservoir to eruption in silicic systems: the Li elemental and isotopic record from rhyolitic melt inclusions and host quartz in a

Yellowstone rhyolite. *Geochimica et Cosmochimica Acta* 326, 56-76. https://doi.org/10.1016/j.gca.2022.03.037.

Noble, D. C., McKee, E. H., Farrar, E. & Petersen, U. (1974). Episodic Cenozoic volcanism and tectonism in the Andes of Peru. *Earth and Planetary Science Letters* 21, 213-220. https://doi.org/10.1016/0012-821X(74)90057-0.

Noble, D. C., Vogel, T. A., Peterson, P. S., Landis, G. P., Grant, N. K., Jezek, P. & McKee, E. H. (1984). Rare-element-enriched, S-type ash-flow tufts containing phenocrysts of muscovite, andalusite, and sillimanite, southeastern Peru. *Geology* 12, 35-39. https://doi.org/10.1130/0091-7613(1984)12<35:RSATCP>2.0.CO;2.

Nupen, S. (2019). Mineral Resource Estimates for the Falchani Lithium Project in the Puno District of Peru. Bryanston, 72 pp.

Perez, N. D., Horton, B. K. & Carlotto, V. (2016). Structural inheritance and selective reactivation in the Central Andes: Cenozoic deformation guided by pre-Andean structures in Southern Peru. *Tectonophysics* 671, 264-280. https://doi.org/10.1016/j.tecto.2015.12.031.

Pichavant, M. & Montel, J.-M. (1988). Petrogenesis of a two-mica ignimbrite suite: The Macusani Volcanics, SE Peru. Ea*rth and Environmental Science Transactions of The Royal Society of Edinburgh* 79, 197–207. https://doi.org/10.1017/S0263593300014218.

Pichavant, M., Valencia Herrera, J., Boulmier, S., Briqueu, L., Joron, J. L., Juteau, M., Marin, L., Michard, A., Sheppard, A. M. F., Treuil, M. & Vernet, M. (1987). *The Macusani glasses, SE Peru: evidence of chemical fractionation in peraluminous magmas*. In: Mysen, B.O. (ed.) *Magmatic processes, physicochemical principles*. Geochemical Society Special Publication 1, 359-373.

Pichavant, M., Kontak, D. J., Valencia Herrera, J. & Clark, A. H. (1988a). The Miocene-Pliocene Macusani Volcanics, SE Peru - I. Mineralogy and magmatic evolution of a two-mica aluminosilicate-bearing ignimbrite suite. *Contributions to Mineralogy and Petrology* 100, 300–324. https://doi.org/10.1007/BF00379742.

Pichavant, M., Kontak, D. J., Briqueu, L., Valencia Herrera, J. & Clark, A. H. (1988b). The Miocene-Pliocene Macusani Volcanics, SE Peru - II. Geochemistry and origin of a felsic peraluminous magma. *Contributions to Mineralogy and Petrology* 100, 325–338. https://doi.org/10.1007/BF00379742.

Pichavant, M., Erdmann, S., Kontak, D. J., Michaud, J. & Villaros, A. (2024a). Trace element partitioning in strongly peraluminous rare-metal silicic magmas – Implications for fractionation processes and for the origin of the Macusani Volcanics (SE Peru). *Geochimica et Cosmochimica Acta* 365, 229–252. https://doi.org/10.1016/j.gca.2023.11.021.

Pichavant, M., Villaros, A., Michaud, J. & Scaillet, B. (2024b). Granite magmatism and mantle filiation. *European Journal of Mineralogy* 36, 225–246. https://doi.org/10.5194/ejm-36-225-2024.

Poupeau, G., Sabil, N., Villa, I. M., Bigazzi, G., Vatin-Perignon, N., Flores, P., Pereyra, P., Salas, G. & Arroyo, G. (1992). Fission-track and K-Ar ages of "macusanite" obsidian glasses, (SE Peru): Geodynamic implications. *Tectonophysics* 205, 295-305. https://doi.org/10.1016/0040-1951(92)90432-6.

Poupeau, G., Labrin, E., Sabil, N., Bigazzi, G., Arroyo, G. & Vatin-Pérignon, N. (1993). Fission-track dating of 15 macusanite glass pebbles from the Macusani Volcanic Field (SE Peru). *Nuclear Tracks and Radiation Measurements* 21, 449–506. https://doi.org/10.1016/1359-0189(93)90189-G.

Qinhua, X. & Aizhen, Y. (1991). Hydrothermal synthesis and crystallization of zeolites. *Progress in Crystal Growth and Characterization of Materials* 21, 29-70. https://doi.org/10.1016/0960-8974(91)90007-Y.

Raczek, I., Stoll, B., Hofmann, A. W. & Jochum K. P. (2001). High-precision trace element data for the USGS reference materials BCR-1, BCR-2, BHVO-1, BHVO-2, AGV-1, AGV-2, DTS-1, DTS-2, GSP-1 and GSP-2 by ID-TIMS and MIC-SSMS. *Geostandards Geoanalytical Research* 25, 77–86. https://doi.org/10.1111/j.1751-908X.2001.tb00789.x.

Ramos, V. A. (2008). The basement of the Central Andes: the Arequipa and related terranes. *Annual Review on Earth and Planetary Sciences* 36, 289-324. https://doi.org/10.1146/annurev.earth.36.031207.124304.

Ramos, V. A. (2018). Tectonic evolution of the central Andes: From terrane accretion to crustal delamination. In: Zamora, G., McClay, K. M. & Ramos, V. (eds.) *Petroleum basins and hydrocarbon potential of the Andes of Peru and Bolivia*. The American Association of Petroleum Geologists Memoir 117, 1–34. https://doi.org/10.1306/13622115M1172855.

Reitsma, M. J. (2012). Reconstructing the Late Paleozoic–Early Mesozoic Plutonic and Sedimentary Record of South-East Peru: Orphaned Back-arcs Along the Western Margin of Gondwana. Doctoral dissertation, Terre & Environment, University of Geneva, Switzerland.

Rodríguez, R., Choquehuanca, S., Muñoz, L., Gómez, W., Martínez, J., Soberon, D. & Serret, S. (2015). Mapa geológico del cuadrángulo de Corani - Hoja 28u2 Carta Geológica Nacional Digital Escala 1: 50 000: Instituto Geológico Minero y Metalúrgico, scale 1:50,000.

Rodríguez, R., Choquehuanca, S., Sánchez, E., Fabián, C. & Del Castillo, B. (2021). Geología de los cuadrángulos de Macusani (hojas 29v1, 29v2, 29v3, 29v4) y Limbani (hojas 29x1, 29x2, 29x3, 29x4). Instituto Geológico, Minero y Metalúrgico, Boletin Serie L4, 82 pp.

Rollinson, H. & Pease, V. (2021). *Using Geochemical Data To Understand Geological Processes*, 2nd edition. Cambridge University Press.

Romer, R., Meixner, A. & Förster, H.-J. (2014). Lithium and boron in late-orogenic granites – Isotopic fingerprints for the source of crustal melts? *Geochimica et Cosmochimica Acta* 131, 98-114. https://doi.org/10.1016/j.gca.2014.01.018.

Rosenberg, C. L. & Handy, M. R. (2005) Experimental deformation of partially melted granite revisited: implications for the continental crust. *The Journal of Metamorphic Geology* 23, 19–28. https://doi.org/10.1111/j.1525-1314.2005.00555.x.

Rubin, J. N., Henry, C. D. & Price, J. G. (1993). The mobility of zirconium and other "immobile" elements during hydrothermal alteration. *Chemical Geology* 110, 29-47. https://doi.org/10.1016/0009-2541(93)90246-F.

Rudnick, R. L. & Gao, S. (2014). Composition of the Continental Crust. In: Holland, H.D. & Turekian, K.K. (eds.) *Treatise on geochemistry*, 2nd edn, Amsterdam, Elsevier, 1–51. https://doi.org/10.1016/B978-0-08-095975-7.00301-6.

Salisbury, M. J., Jicha, B. R., de Silva, S. L., Singer, B. S., Jiménez, N. C. & Ort, M. H. (2011). ^{40}Ar/^{39}Ar chronostratigraphy of Altiplano-Puna Volcanic Complex ignimbrites reveals the development of a major magmatic province. *Geological Society of America Bulletin* 123, 821–840. https://doi.org/10.1130/B30280.1.

Salisbury, M., Jiménez, N., & Barfod, D. (2022). ^{40}Ar/^{39}Ar ages and geochemistry of the intersalar range of the Bolivian Altiplano: A volcanological transect spanning the arc and reararc of the Central Andean Plateau. *Frontiers in Earth Science Section Geochemistry* 10:23. https://doi.org/10.3389/feart.2022.917488.

Salters, V. J. & Stracke, A. (2004). Composition of the depleted mantle. *Geochemistry, Geophysics, Geosystems* 5, Q05B07. https://doi.org/10.1029/2003GC000597.

Sanandres-Flores, M. K. (2024). ^{40}Ar/^{39}Ar Geochronology of the lithium-rich tuff in the Macusani Volcanic field, Oriental Cordillera, Peru. [Undergraduate Thesis, Pontifical Catholic University of Peru]. PUCP Campus Repository. http://hdl.handle.net/20.500.12404/28843.

Sánchez, A. W. & Zapata, A. A. (2003). Memoria descriptiva de la revisión y actualización de los cuadrángulos de Río Picha (25-p), Timpia (25-q), Chuanquiri (26-p), Quillabamba (26-q), Quebrada Honda (26-r), Parobamba (26-s), Pacaypata (27-p), Machupicchu (27-q), Urubamba (27-r), Calca (27-s), Chotachaca (27-t), Quincemil (27-u), Ocongate, Corani (28-u) y Ayapata (28-v). Escala 1:100 000. INGEMET. https://hdl.handle.net/20.500.12544/2073 (accessed 9 October 2024)

Sandeman, H. A., Clark, A. H. & Farrar, E. (1995). An integrated tectono-magmatic model for the evolution of the southern Peruvian Andes (13-20°S) since 55 Ma. *International Geology Review* 37, 1039–1073. https://doi.org/10.1080/00206819509465439.

Sandeman, H. A., Clark, A. H., Farrar, E. & Arroyo-Pauca, G. (1997). Lithostratigraphy, petrology and ^{40}Ar-^{39}Ar geochronology of the Crucero Supergroup, Puno Department, SE Peru. *Journal of South American Earth Sciences* 10, 223–245. https://doi.org/10.1016/S0895-9811(97)00023-0.

Scheuber, E., Mertmann, D., Age, H., Silva, P., Heubeck, C., Reutter, K.-J. & Jacobshagen. V. (2006). *Exhumation and Basin Development Related to Formation of the Central Andean Plateau, 21° S.* In: Oncken, O., Chong, G., Franz, G., Giese, P., Götze, H.-J., Ramos, V., Strecker, M. & Wigger, P. (eds.) *The Andes Active, Frontiers in Earth Sciences*. Springer, Berlin. https://doi.org/10.1007/978-3-540-48684-8_13.

Schmidt, K., Bau, M., Hein, J. R. & Koschinsky, A. (2014). Fractionation of the geochemical twins Zr-Hf and Nb-Ta during scavenging from seawater by hydrogenetic ferromanganese crusts, *Geochimica et Cosmochimica Acta* 140, 468-487. https://doi.org/10.1016/j.gca.2014.05.036.

Segovia-More, M. K., Torró, L., Villanova-de-Benavent, C., Ramírez-Briones, J., Vallance, J., Monnier, L., Laurent, O., Salvi, S., Baby, P., Proenza, J. A. & Nieto, F. (2023). High-resolution mineralogy of Lithium-rich Tuff from the Macusani Volcanic Field, Puno, Peru. Proceedings of the 17th SGA Biennial Meeting 1, 303-306.

Sempere, T., Carlier, G., Soler, P., Fornari, M., Carlotto, V., Jacay, J., Arispe, O., Néraudeau, D., Cárdenas, J., Rosas, S., & Jiménez, N. (2002). Late Permian-Middle Jurassic lithospheric thinning in Peru and Bolivia, and its bearing on Andean-age tectonics. *Tectonophysics* 345, 153–181. https://doi.org/10.1016/S0040-1951(01)00211-6.

Shand, S. J. (1943). *The eruptive rocks*. Second edition, John Wiley, New York, 444 pp.

Shaw, R., Goodenough, K., Deady, E., Nex, P., Ruzvidzo, B., Rushton, J. & Pearson, M. (2022). The magmatic–hydrothermal transition in lithium pegmatites: Petrographic and geochemical characteristics of pegmatites from the Kamativi area, Zimbabwe. *The Canadian Mineralogist* 60, 957-987. https://doi.org/10.3749/canmin.2100032.

Siebel, W., Schnurr, W. B. W., Hahne, K., Kraemer, B., Trumbull, R. B., van den Bogaard, P. & Emmermann, R. (2001). Geochemistry and isotope systematics of small- to medium-volume Neogene–Quaternary ignimbrites in the southern central Andes: evidence for derivation from andesitic magma sources. *Chemical Geology* 171, 213–237. https://doi.org/10.1016/S0009-2541(00)00249-7.

Spikings, R., Reitsma, M. J., Boekhout, F., Mišković, A., Ulianov, A., Chiaradia, M., Gerde, A. & Schaltegger, U. (2016). Characterization of Triassic rifting in Peru and implications for the early disassembly of western Pangaea. *Gondwana Research* 35, 124–143. https://doi.org/10.1016/j.gr.2016.02.008.

Starkey, H. C. (1982). The Role of Clays in Fixing Lithium: Geological Survey Bulletin 1278-F US Gov, Virginia, 20 p.

Steiger, R. H. & Jager, E. (1977). Subcommission on geochronology: Convention of the use of decay constants in geo- and cosmochronology. *Earth and Planetary Science Letters* 36, 359-362. https://doi.org/10.1306/St6398C6.

Steinmetz, L. (2017). Lithium- and boron-bearing brines in the Central Andes: Exploring hydrofacies on the eastern Puna plateau between 23° and 23°30′S. *Mineralium Deposita* 52, 35–50. https://doi.org/10.1007/s00126-016-0656-x.

Sundell, K., Saylor, J., Lapen, T., Styron, R., Villarreal, D., Usnayo, P. & Cárdenas, J. (2019). Peruvian Altiplano stratigraphy highlights along-strike variability in foreland basin evolution of the Cenozoic Central Andes. *Tectonics* 37, 1876-1904. https://doi.org/10.1029/2017TC004775.

Tartèse, R. & Boulvais, P. (2010). Differentiation of peraluminous leucogranites "en route" to the surface. *Lithos* 114, 353-368. https://doi.org/10.1016/j.lithos.2009.09.011.

Tavazzani, L., Economos, R. C., Peres, S., Demarchi, G., Sinigoi, S. & Bachmann, O. (2024). The role of latent heat buffering in the generation of high-silica rhyolites. *Journal of Petrology* 65, egae072. https://doi.org/10.1093/petrology/egae072.

Thomas, R. & Davidson, P. (2012). Water in granite and pegmatite-forming melts. *Ore Geology Reviews* 46, 32–46. https://doi.org/10.1016/j.oregeorev.2012.02.006.

Torró, L., Villanova-de-Benavent, C., Monnier, L., Laurent, O., Segovia-More, M. K., Sanandres-Flores, M., Ramírez-Briones, J., Vallance, J., Salvi, S., Baby, P., Proenza, J. A. & Nieto, F. (2023). Lepidolite and zinnwaldite mineralization in 'lithium-rich tuffs' from the Macusani Volcanic Field, Puno, Peru. Proceedings of the 17th SGA Biennial Meeting 1, 319-322.

Townsend, M., Huber, C., Degruyter, W. & Bachmann, O. (2019). Magma chamber growth during intercaldera periods: Insights from thermo-mechanical modeling with applications to Laguna del Maule, Campi Flegrei, Santorini, and Aso. *Geochemistry, Geophysics, Geosystems* 20, 1574–1591. https://doi.org/10.1029/2018GC008103.

Troch, J., Huber, C. & Bachmann, O. (2022). The physical and chemical evolution of magmatic fluids in near-solidus silicic magma reservoirs: Implications for the formation of pegmatites. *American Mineralogist* 107, 190–205. https://doi.org/10.2138/am-2021-7915.

Ulrich, T. & Heinrich, C. A. (2002) Geology and alteration geochemistry of the porphyry Cu-Au deposit at Bajo de la Alumbrera, Argentina. *Economic Geology* 97, 1865–1888. https://doi.org/10.2113/gsecongeo.97.8.1865

Valencia, J. & Arroyo, G. (1985). Geochemical aspects of the uranium occurrences of Macusani, Puno (Peru). International Atomic Energy Agency, Uranium Deposits in Volcanic Rocks, Proceedings of a Technical Committee Meeting, 275–288.

Vermeesch, P. (2018). IsoplotR: A free and open toolbox for geochronology. Geoscience Frontiers 9, 1479–1493. https://doi.org/10.1016/j.gsf.2018.04.001.

Villaros, A. & Pichavant, M. (2019). Mica-liquid trace elements partitioning and the granite-pegmatite connection: The St-Sylvestre complex (Western French Massif Central). *Chemical Geology* 528, 119265. https://doi.org/10.1016/j.chemgeo.2019.07.040.

Wang, R., Richards, J. P., Zhou, L.-M., Hou, Z.-Q., Stern, R. A., Creaser, R. A. & Zhu, J.-J. (2021). The role of Indian metasedimentary basement in the formation of thick crust and peraluminous magmatism in the Gangdese belt. *Geological Society of America Bulletin* 133, 1107-1125. https://doi.org/10.1130/B35514.1.

Ward, K. M., Zandt, G., Beck, S. L., Wagner, L. S. & Tavera, H. (2016). Lithospheric structure beneath the northern Central Andean Plateau from the joint inversion of ambient noise and earthquake-generated surface waves. *Journal of Geophysical Research: Solid Earth* 121, 8217–8238. https://doi.org/10.1002/2016JB013237.

Wasserburg, G. J., Jacobsen, S. B., DePaolo, D. J., McCulloch, M. T. & Wen, J. (1981). Precise determinations of Sm/Nd ratios, Sm and Nd isotopic abundances in standard solutions. *Geochimica et Cosmochimica Acta* 45, 2311–2323. https://doi.org/10.1016/0016-7037(81)90085-5.

Watson, B. & Harrison, M. (1983). Zircon saturation revisited: Temperature and composition effects in a variety of crustal magma types. *Earth and Planetary Science Letters* 64, 295-304. https://doi.org/10.1016/0012-821X(83)90211-X.

Winter, J. D. (2014). *Principles of Igneous and Metamorphic Petrology*. Pearson New International Edition. Pearson Education Limited, Harlow, UK.

Wolf, M. B., Romer, R. L. & Glodny, J. (2019). Isotope disequilibrium during partial melting of metasedimentary rocks. *Geochimica et Cosmochimica Acta* 257, 163–183. https://doi.org/10.1016/j.gca.2019.05.008.

Wörner, G., Schildgen, T. F. & Reich, M. (2018). The Central Andes: Elements of an extreme land. *Elements* 14, 225–230. https://doi.org/10.2138/gselements.14.4.225.

Wörner, G., Hammerschmidt, K., Henjes-Kunst, F., Lezaun, J. & Wilke, H. (2000). Geochronology (^{40}Ar/^{39}Ar, K-Ar and He-exposure ages) of Cenozoic magmatic rocks from Northern Chile (18–22°): Implications for magmatism and tectonic evolution of the central Andes. *Revista Geológica de Chile* 27, 205–240.

Zartman, R. E. & Doe, B. R. (1981). Plumbotectonics—the model. *Tectonophysics* 75, 135–162. https://doi.org/10.1016/0040-1951(81)90213-4.

FIGURE CAPTIONS

Fig. 1 Location map of the Macusani Volcanic Field within the Neogene Ignimbrite Province of the Central Andes extending between 13 °S and 28 °S (Sandeman et al., 1997; Wörner et al., 2018). Structural boundaries between morphotectonic domains (Laubacher, 1978; Scheuber et al., 2006; Armijo et al., 2015; Baby et al., 2018) and the projection of the three Arequipa-Antofalla basement block domains (Loewy et al., 2004) are shown. The location of samples analyzed by previous authors with Sr and Nd isotope data used in our discussion is provided (Pichavant et al., 1987, 1988b; Loewy et al., 2004; Carlier et al., 2005; Kay et al., 2010; Reitsma, 2012; Kato, 2013; Martínez et al. 2019; Harlaux et al., 2021; DIGIS Team, 2023).

Fig. 2 Simplified geological map of the Macusani Volcanic Field and adjacent areas in the Eastern Cordillera modified from López (1996), Sandeman et al. (1997), Choquehuanca et al. (2015), and Rodríguez et al. (2015). Dotted patterns indicate intrusive rocks. The location of samples analyzed for whole rock geochemistry in this and previous studies is indicated. References: [1] Linck (1926); [2] Francis (1953); [3] Martin & de Sitter-Koomans (1955); [4] Elliott & Moss (1965); [5] Barnes et al. (1970); [6] Noble et al. (1984); [7] Valencia & Arroyo (1985); [8] Pichavant et al. (1987); [9] Pichavant et al. (1988b); [10] Poupeau et al. (1992); [11] MacDonald et al. (1992); [12] Craig et al. (2010); [13] Pichavant et al. (2024a).

Fig. 3 (a) S-N cross section of the Li-ore bearing units at the Falchani Lithium Project (modified from Nupen, 2019). (b) Aspect of the Upper Breccia in a drill core sample, with a white color and clayey, brecciated texture. (c-d) Aspect of the Lithium-rich Tuff in hand sample; note the mm-scale, alternating slightly darker and lighter laminae defining anastomosed to contorted banding and slump structures. (e) Detail of dark Li-F mica crystal clasts scattered in a sample of Lithium-rich Tuff.

Fig. 4 Major elements bivariate plots showcasing analyzed samples from the Macusani Volcanic Field. (a) Na_2O+K_2O *vs.* SiO_2 diagram. (b) TAS diagram of Le Maitre et al. (1989); note that in (b), data have been recalculated to 100% on an anhydrous (volatile-free) basis. (c) $Al_2O_3/(CaO+Na_2O+K_2O)$ *vs.* $Al_2O_3/(Na_2O+K_2O)$ diagram after Shand (1943). (d) B *vs.* A diagram after Debon & Le Fort (1983). Compositional fields of highly evolved rare metal-rich granites, highly evolved volcanic rocks, evolved granites, muscovite-biotite and muscovite granites, and biotite granites are after Michaud et al. (2021). Compositional fields of other volcanic and intrusive rocks in the study area are plotted for comparison. References: [1] Linck (1926); [2] Francis (1953); [3] Martin & de Sitter-Koomans (1955); [4] Elliott & Moss (1965); [5] Barnes et al. (1970); [6] Noble et al. (1984); [7] Arribas & Figueroa (1985); [8] Valencia & Arroyo (1985); [9] Pichavant et al. (1987); [10] Pichavant et al. (1988b); [11] Poupeau et al. (1992); [12] Harlaux et al. (2021); [13] Pichavant et al. (2024a).

Fig. 5 Normalized composition of volcanogenic rocks from the Macusani Volcanic Field. (a) Upper continental crust-normalized multi-element spider diagrams; upper continental crust values after Rudnick & Gao (2003). (b) Chondrite-normalized REY spider diagrams; C1 chondrite values after McDonough & Sun (1995). Median values are represented as thick lines, individual analyses as thinner lines, and compositional ranges as polygons. References: [1] Linck (1926); [2] Martin & de Sitter-Koomans (1955); [4] Elliott & Moss (1965); [5] Barnes et al. (1970); [6] Noble et al. (1984); [7] Arribas and Figueroa (1985); [8] Valencia & Arroyo (1985); [9] Pichavant et al.

(1988b); [10] Poupeau et al. (1992); [11] MacDonald et al. (1992); [12] Craig et al. (2010); [13] Pichavant et al. (2024a).

Fig. 6 Isocon diagram (Grant 1986) for (a) Upper Breccia and Lower Breccia and (b) Lithium-rich Tuff from the Falchani Lithium Project in the Macusani Volcanic Field. In the insets, the vertical scales are enhanced for clarity. See text for details.

Fig. 7 Whole-rock radiogenic Pb isotopes of volcanogenic and intrusive rocks from the Macusani Volcanic Field (this and previous studies) and other key igneous and basement entities in the Central Andes including those of the Arequipa-Antofalla Basement Block (AABB) and Ordovician metapelites of the Sandia Formation in the Macusani Structural Zone. The lower and upper crust, and mantle Pb growth curves are generated by the plumbotectonics model version 2 (Zartman & Doe, 1981). Analytical uncertainties are smaller than the size of the points. References: [1] Pichavant et al. (1987); [2] Pichavant et al. (1988b); [3] Loewy et al. (2004); [4] Harlaux et al. (2021).

Fig. 8 Whole-rock radiogenic Sr and Nd isotopes of volcanogenic and intrusive rocks from the Macusani Volcanic Field (this and previous studies) and other key igneous and basement entities in the Central Andes including those of the Arequipa-Antofalla Basement Block (AABB) and Ordovician metapelites of the Sandia Formation in the Macusani Structural Zone. (a-b) Strontium and Nd isotope compositions in the $^{87}Sr/^{86}Sr_{(t)}$ *vs.* $^{143}Nd/^{144}Nd_{(t)}$ diagram. All data were recalculated to 8.9 Ma with the exception of macusanite, for which $^{143}Nd/^{144}Nd_{(t)}$ cannot be calculated since Nd contents are not provided in the referenced works. (c) Whole rock Rb-Sr isochrone for four samples of Lithium-rich Tuff rocks calculated using IsoplotR (Vermeesch, 2018). Two samples (2021-MAC-031 and 2021-MAC-038) were excluded because they fall far from the Rb-Sr isochrone. (d)

Sm/Nd T_{DM} *vs.* ε_{Nd}^{0} diagram. Analytical uncertainties are smaller than the size of the points. References: [1] Pichavant et al. (1987); [2] Pichavant et al. (1988b); [3] Loewy et al. (2004); [4] Carlier et al. (2005); [5] Kay et al. (2010); [6] Reitsma (2012); [7] Kato (2013); [8] Martínez et al. (2019); [9] Harlaux et al. (2021); [10] DIGIS Team (2023). Abbreviations: DM—depleted mantle (Salters & Stracke, 2004). CHUR—chondritic uniform reservoir (Goldstein et al., 1984).

Fig. 9 Geochemical composition of samples from the Macusani Volcanic Field in terms of (a) Zr/Hf *vs.* Nb/Ta and (b) Mg/Li *vs.* La/Ta. The compositional fields in (a) are after Ballouard et al. (2016), and compositional fields in (b) are after Shaw et al. (2022). CHARAC field is after Schmidt et al. (2014).

Fig. 10 Strontium and Nd isotope ratios corrected to 8.9 Ma of volcanogenic and intrusive rocks from the Macusani Volcanic Field and the San Rafael Intrusive Complex and compositional fields of regional rocks discussed in the main text. The compositional field of Proterozoic and Paleozoic paragneiss from the Puna Plateau and Sierras Pampeanas encompasses 80% of the corresponding data presented in Figure 8, thereby effectively excluding outliers. The selected crustal rock end-members represent average isotopic values of Proterozoic and Paleozoic paragneiss in the Puna plateau and Sierras Pampeanas (S1; DIGIS Team, 2023) and Ordovician metapelite of the Sandia Formation (S2; Harlaux et al., 2021). The selected mantle-derived end-member is a late Miocene (7.51 ± 0.05 Ma; $^{40}Ar/^{39}Ar$ phlogopite date, error 2σ) olivine minette from the Eastern Cordillera (Carlier et al. 2005). The employed models assume complete chemical mixing of two end-members resulting in a homogeneous mixture (i.e. hybridization; Heinonen et al., 2021). Percentages represent the fraction of the mantle-derived end-member. References: [1] Carlier et al. (2005); [2]

Reitsma (2012); [3] Martínez et al. (2019); [4] Harlaux et al. (2021); [5] DIGIS Team (2023). Abbreviations: DM—Depleted mantle; EM—Enriched mantle.

Fig. 11 Bivariant plots of Rb *vs.* elements that behaved as incompatible in parental magmas to Macusani Formation rocks including (a) Li, (b) Be, (c) B, (d) F, (e) Cs, (f) Sn, (g) W, (h) Nb, and (i) Ta, and (j) Nb/Ta ratio. Fractional crystallization is modeled as outlined in Rollinson & Pease (2021). The percentages indicate the proportion of crystal fractionation. Experimental mineral/melt partition coefficients in felsic peraluminous magmas of Villaros & Pichavant (2019) and Pichavant et al. (2024a) were employed. Thick lines represent models with a fractionated assemblage corresponding to average modal proportions of phenocrysts in ash-flow tuff as estimated by Pichavant et al. (1988a) [quartz (0.330), alkali feldspar (0.367), plagioclase (0.239), biotite (0.051), andalusite (0.007), and muscovite (0.006)]. Thin gray lines represent the six different phenocryst modes considered by Pichavant et al. (2024a) to account for the effect of antecryst recycling in long-lived, large-volume silicic systems. Curves with different colors represent melt evolution during crystallization-differentiation when initial melts are established as the least evolved glass in Macusani Formation ash-flow tuff (black line; Model 1) or the average of glass in the most evolved Macusani Formation ash-flow tuff (pale orange line; Model 2). The compositions of starting melts with an additional 20% mantle-derived contribution (Model 3; see calculation in Figs. S5 and S6) are also considered for the aforementioned least (Model 3a; purple line) and most (Model 3b; dark orange line) evolved glasses. Given the little variation in the final products of hybridization with a mantle-derived component for the different considered degrees of fractional crystallization, a 30 % of crystallization was chosen as it represents and intermediate, plausible value. All Lithium-rich Tuff samples with LOI > 2.7 wt % or plotting outside the Rb-Sr isochrone were not considered in the plots. References: [1] Barnes et al. (1970); [2] Pichavant et al. (1987); [3] Pichavant et al. (1988b); [4] Craig et al. (2010); [5] Pichavant et al. (2024a).

Fig. 12 Bivariant plots of Rb *vs.* elements that behaved as compatible in parental magmas to Macusani Formation rocks including (a) Sr, (b) Ba, (c) Ti, and (d) Pb. Fractional crystallization (curves) models were calculated using the same parameters and references as in Figure 11. Physical segregation (accumulation; arrows) of crystals was calculated by adding zinnwaldite, lepidolite, and feldspars at increasing 2% proportions to a glass with the average composition of the most evolved macusanite specimens (JV3, CH1, and CH0). The composition of Li-F micas was extracted from Torró et al. (2023) and the composition of feldspars was extracted from the most evolved feldspars in Macusani Formation ash-flow tuff as reported by Pichavant et al. (2024a).

Fig. 13 T_{REE} (Montel, 1993) *vs.* T_{Zr} (Watson & Harrison, 1983) plot for volcanogenic and intrusive units in the Macusani Volcanic Field and intrusive rocks in the San Rafael intrusive complex. References: [1] Pichavant et al. (1987); [2] Pichavant et al. (1988b); [3] Harlaux et al. (2021).

Fig. 14 Transcrustal magmatic model in the Eastern Cordillera of southern Peru for the genesis of magmas parental to Li-ore units in the Falchani Lithium Project. Mantle-derived input and different crustal magmatic reservoirs beneath the Macusani Volcanic Field are inspired in Pichavant et al. (1988b, 2024b). Lithospheric mantle, underplated basalts, and mafic granulites in accordance to the high wave speed anomaly reported by Garzione et al. (2017) and petrological interpretations of Carlier et al. (2005). The ~55-65 km crustal thickness during the late Miocene is based on Garzione et al. (2017). This overthickened crust is likely the result of crustal-scale thrust stacking (Perez et al., 2016; Baby et al., 2018). Fractional crystallization drove volatile exsolution and, potentially, fluid migration through the crystal mush, concentrating incompatible lithophile elements at the magma chamber roof. Pre-eruptive crystallization of Li-F micas retained lithium in the system, while their subsequent entrainment in the erupted products led to the high Li contents in the Falchani deposit. References: [1] Pichavant et al. (1988a); [2] Pichavant et al. (1988b); [3] Carlier et al. (2005); [4] Tartèse & Boulvais (2010); [5] Garzione et al. (2017); [6] Pichavant et al. (2024a).

TABLE CAPTIONS

Table 1 Whole-rock radiogenic Sr, Nd, and Pb isotope results.

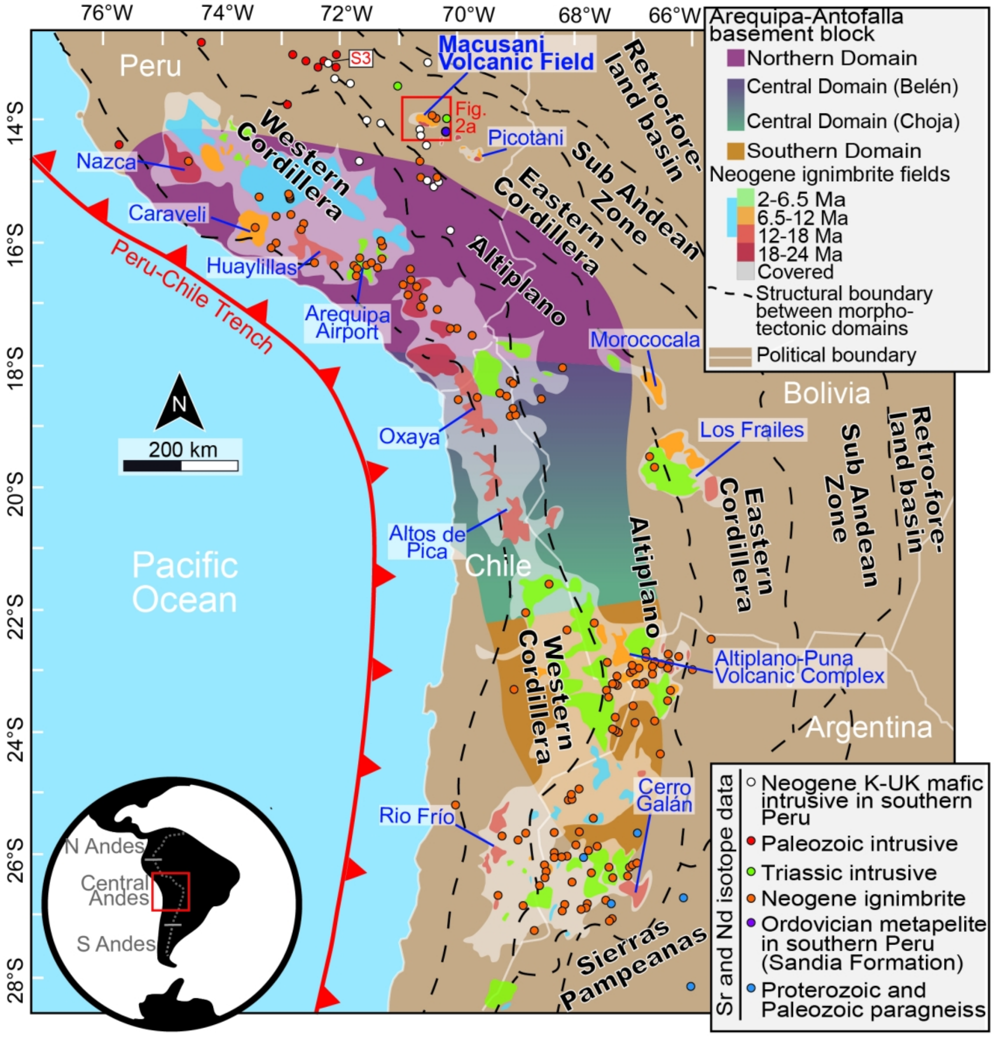

Fig. 1 Location map of the Macusani Volcanic Field within the Neogene Ignimbrite Province of the Central Andes extending between 13 °S and 28 °S (Sandeman et al., 1997; Wörner et al., 2018). Structural boundaries between morphotectonic domains (Laubacher, 1978; Scheuber et al., 2006; Armijo et al., 2015; Baby et al., 2018) and the projection of the three Arequipa-Antofalla basement block domains (Loewy et al., 2004) are shown. The location of samples analyzed by previous authors with Sr and Nd isotope data used in our discussion is provided (Pichavant et al., 1987, 1988b; Loewy et al., 2004; Carlier et al., 2005; Kay et al., 2010; Reitsma, 2012; Kato, 2013; Martínez et al. 2019; Harlaux et al., 2021; DIGIS Team, 2023).

165x171mm (300 x 300 DPI)

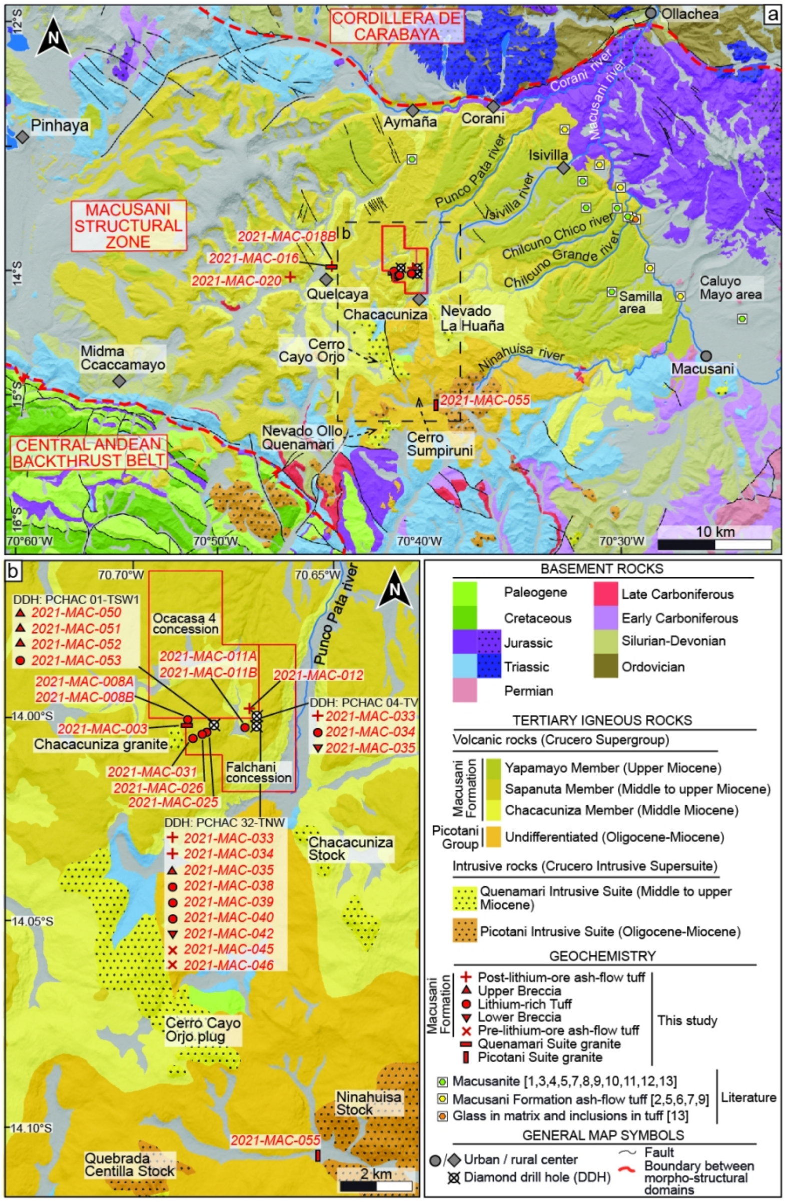

Fig. 2 Simplified geological map of the Macusani Volcanic Field and adjacent areas in the Eastern Cordillera modified from López (1996), Sandeman et al. (1997), Choquehuanca et al. (2015), and Rodríguez et al. (2015). Dotted patterns indicate intrusive rocks. The location of samples analyzed for whole rock geochemistry in this and previous studies is indicated. References: [1] Linck (1926); [2] Francis (1953); [3] Martin & de Sitter-Koomans (1955); [4] Elliott & Moss (1965); [5] Barnes et al. (1970); [6] Noble et al. (1984); [7] Valencia & Arroyo (1985); [8] Pichavant et al. (1987); [9] Pichavant et al. (1988b); [10] Poupeau et al. (1992); [11] MacDonald et al. (1992); [12] Craig et al. (2010); [13] Pichavant et al. (2024a).

188x288mm (150 x 150 DPI)

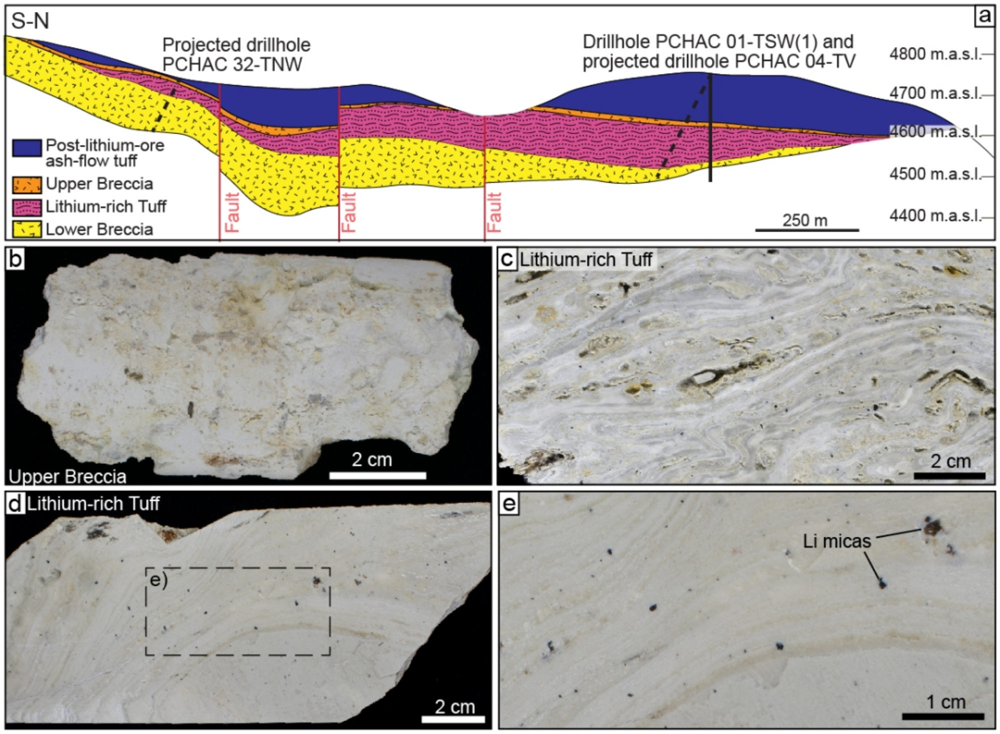

Fig. 3 (a) S-N cross section of the Li-ore bearing units at the Falchani Lithium Project (modified from Nupen, 2019). (b) Aspect of the Upper Breccia in a drill core sample, with a white color and clayey, brecciated texture. (c-d) Aspect of the Lithium-rich Tuff in hand sample; note the mm-scale, alternating slightly darker and lighter laminae defining anastomosed to contorted banding and slump structures. (e) Detail of dark Li-F mica crystal clasts scattered in a sample of Lithium-rich Tuff.

207x152mm (150 x 150 DPI)

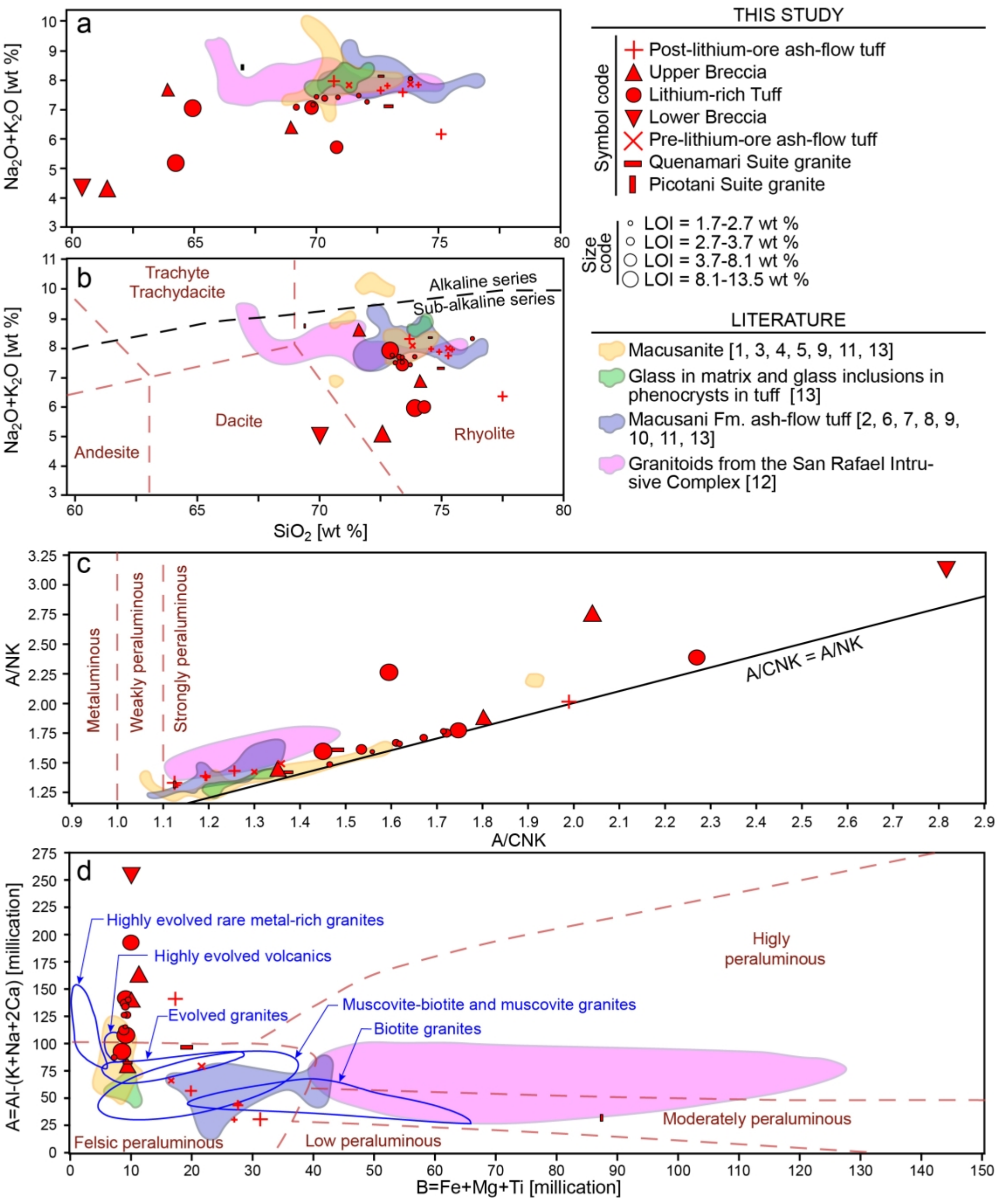

Fig. 4 Major elements bivariate plots showcasing analyzed samples from the Macusani Volcanic Field. (a) Na_2O+K_2O vs. SiO_2 diagram. (b) TAS diagram of Le Maitre et al. (1989); note that in (b), data have been recalculated to 100% on an anhydrous (volatile-free) basis. (c) $Al_2O_3/(CaO+Na_2O+K_2O)$ vs. $Al_2O_3/(Na_2O+K_2O)$ diagram after Shand (1943). (d) B vs. A diagram after Debon & Le Fort (1983). Compositional fields of highly evolved rare metal-rich granites, highly evolved volcanic rocks, evolved granites, muscovite-biotite and muscovite granites, and biotite granites are after Michaud et al. (2021). Compositional fields of other volcanic and intrusive rocks in the study area are plotted for comparison. References: [1] Linck (1926); [2] Francis (1953); [3] Martin & de Sitter-Koomans (1955); [4] Elliott & Moss (1965); [5] Barnes et al. (1970); [6] Noble et al. (1984); [7] Arribas & Figueroa (1985); [8] Valencia & Arroyo (1985); [9] Pichavant et al. (1987); [10] Pichavant et al. (1988b); [11] Poupeau et al. (1992); [12] Harlaux et al. (2021); [13] Pichavant et al. (2024a).

188x225mm (300 x 300 DPI)

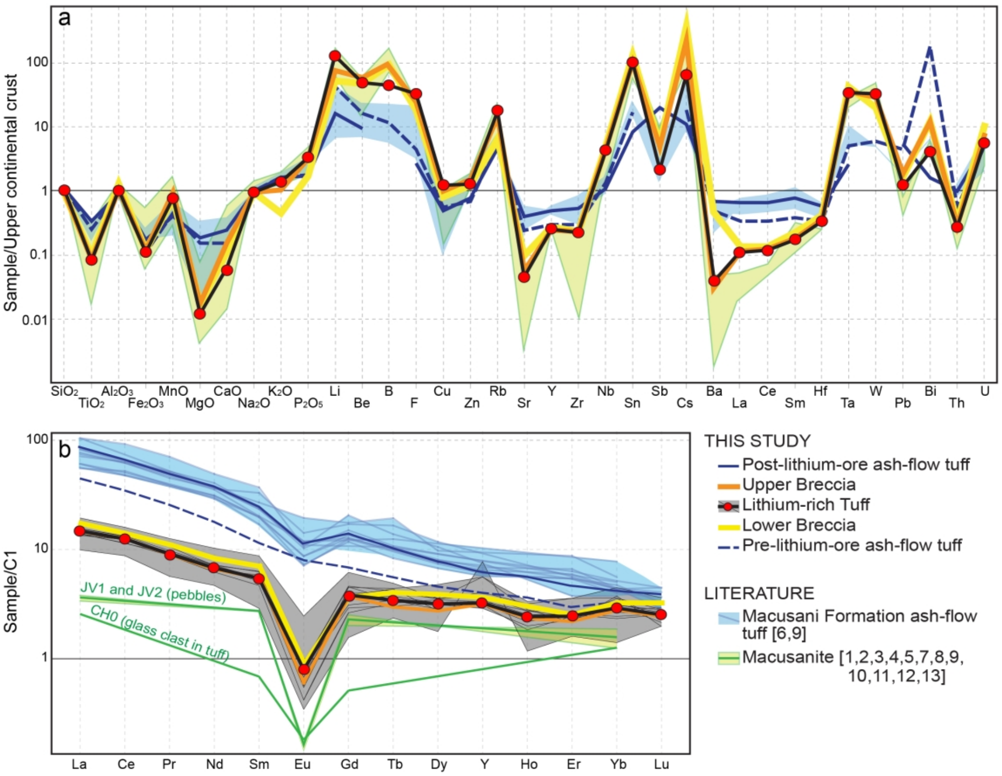

Fig. 5 Normalized composition of volcanogenic rocks from the Macusani Volcanic Field. (a) Upper continental crust-normalized multi-element spider diagrams; upper continental crust values after Rudnick & Gao (2003). (b) Chondrite-normalized REY spider diagrams; C1 chondrite values after McDonough & Sun (1995). Median values are represented as thick lines, individual analyses as thinner lines, and compositional ranges as polygons. References: [1] Linck (1926); [2] Martin & de Sitter-Koomans (1955); [4] Elliott & Moss (1965); [5] Barnes et al. (1970); [6] Noble et al. (1984); [7] Arribas and Figueroa (1985); [8] Valencia & Arroyo (1985); [9] Pichavant et al. (1988b); [10] Poupeau et al. (1992); [11] MacDonald et al. (1992); [12] Craig et al. (2010); [13] Pichavant et al. (2024a).

206x159mm (300 x 300 DPI)

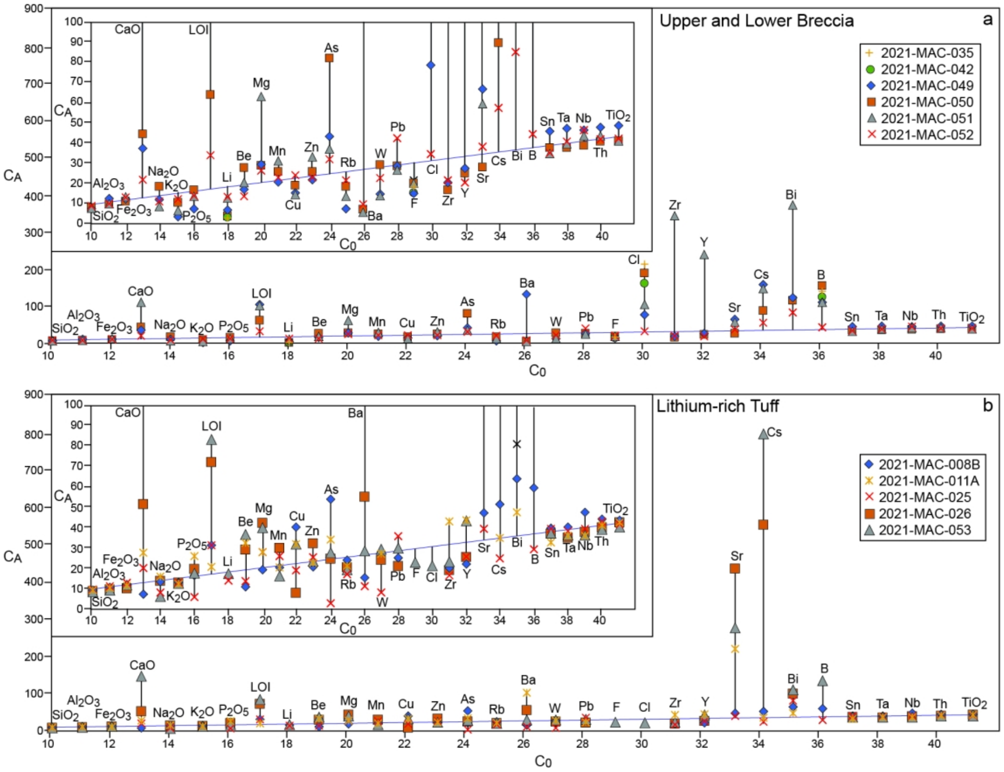

Fig. 6 Isocon diagram (Grant 1986) for (a) Upper Breccia and Lower Breccia and (b) Lithium-rich Tuff from the Falchani Lithium Project in the Macusani Volcanic Field. In the insets, the vertical scales are enhanced for clarity. See text for details.

310x237mm (150 x 150 DPI)

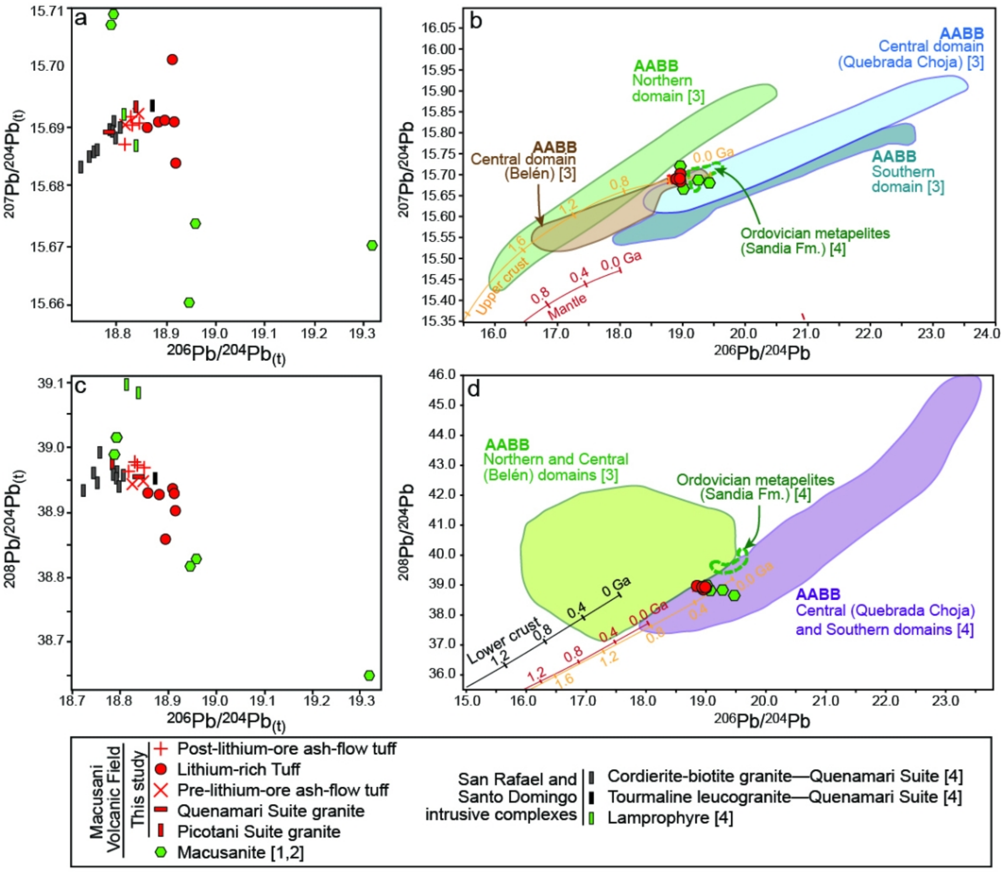

Fig. 7 Whole-rock radiogenic Pb isotopes of volcanogenic and intrusive rocks from the Macusani Volcanic Field (this and previous studies) and other key igneous and basement entities in the Central Andes including those of the Arequipa-Antofalla Basement Block (AABB) and Ordovician metapelites of the Sandia Formation in the Macusani Structural Zone. The lower and upper crust, and mantle Pb growth curves are generated by the plumbotectonics model version 2 (Zartman & Doe, 1981). Analytical uncertainties are smaller than the size of the points. References: [1] Pichavant et al. (1987); [2] Pichavant et al. (1988b); [3] Loewy et al. (2004); [4] Harlaux et al. (2021).

203x177mm (150 x 150 DPI)

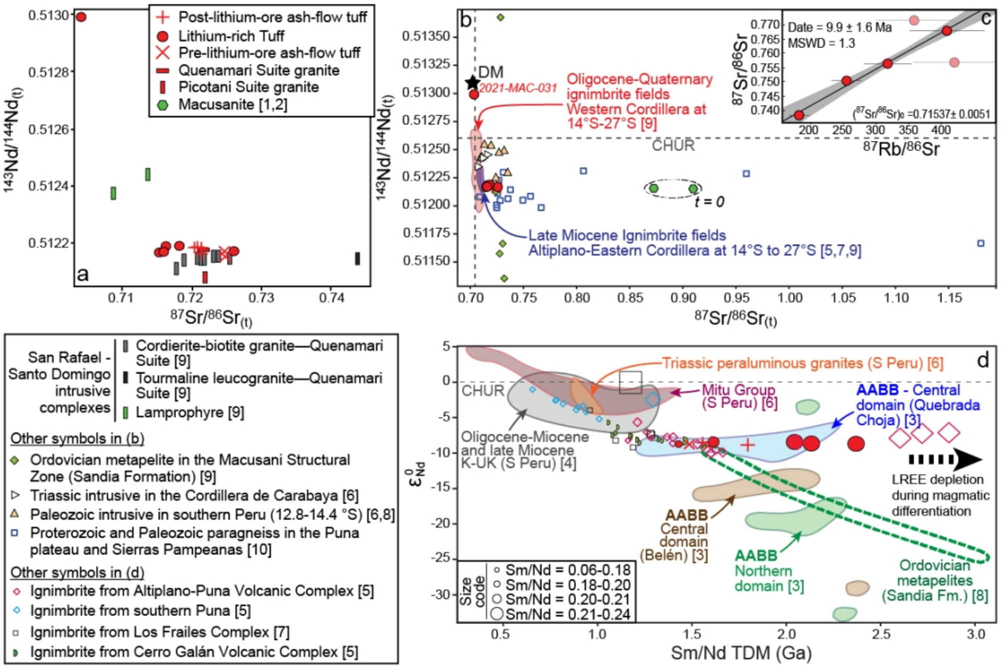

Fig. 8 Whole-rock radiogenic Sr and Nd isotopes of volcanogenic and intrusive rocks from the Macusani Volcanic Field (this and previous studies) and other key igneous and basement entities in the Central Andes including those of the Arequipa-Antofalla Basement Block (AABB) and Ordovician metapelites of the Sandia Formation in the Macusani Structural Zone. (a-b) Strontium and Nd isotope compositions in the ^{87}Sr/^{8}6Sr(t) vs. ^{143}Nd/^{144}Nd(t) diagram. All data were recalculated to 8.9 Ma with the exception of macusanite, for which ^{143}Nd/^{144}Nd(t) cannot be calculated since Nd contents are not provided in the referenced works. (c) Whole rock Rb-Sr isochrone for four samples of Lithium-rich Tuff rocks calculated using IsoplotR (Vermeesch, 2018). Two samples (2021-MAC-031 and 2021-MAC-038) were excluded because they fall far from the Rb-Sr isochrone. (d) Sm/Nd T_{DM} vs. ε_{Nd}^0 diagram. Analytical uncertainties are smaller than the size of the points. References: [1] Pichavant et al. (1987); [2] Pichavant et al. (1988b); [3] Loewy et al. (2004); [4] Carlier et al. (2005); [5] Kay et al. (2010); [6] Reitsma (2012); [7] Kato (2013); [8] Martínez et al. (2019); [9] Harlaux et al. (2021); [10] DIGIS Team (2023). Abbreviations: DM—depleted mantle (Salters & Stracke, 2004). CHUR—chondritic uniform reservoir (Goldstein et al., 1984).

213x141mm (150 x 150 DPI)

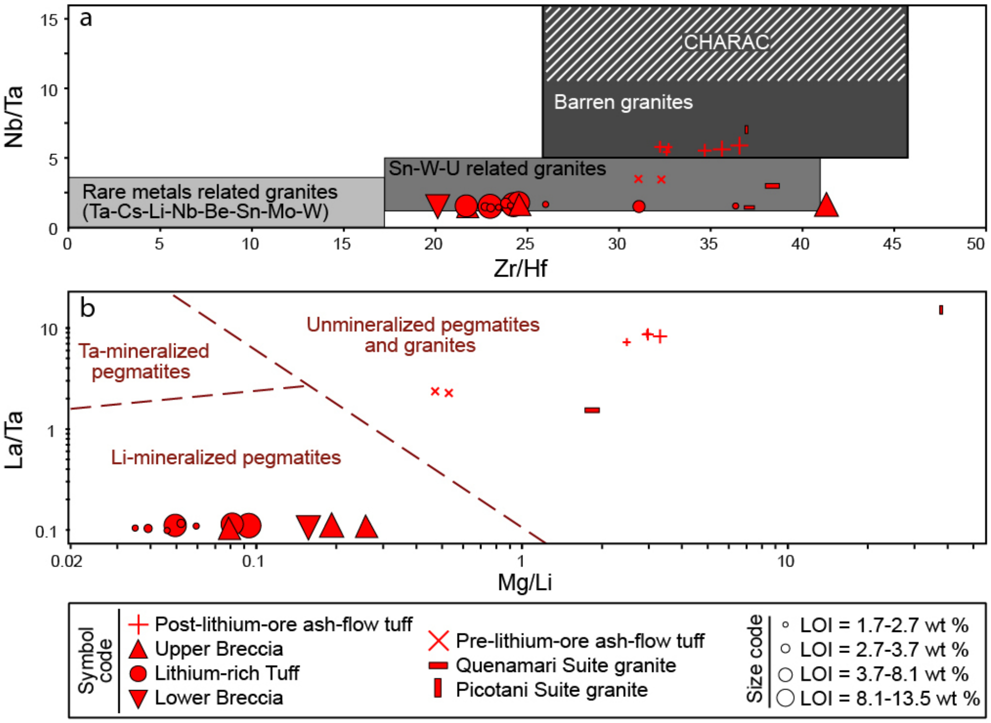

Fig. 9 Geochemical composition of samples from the Macusani Volcanic Field in terms of (a) Zr/Hf vs. Nb/Ta and (b) Mg/Li vs. La/Ta. The compositional fields in (a) are after Ballouard et al. (2016), and compositional fields in (b) are after Shaw et al. (2022). CHARAC field is after Schmidt et al. (2014).

173x125mm (150 x 150 DPI)

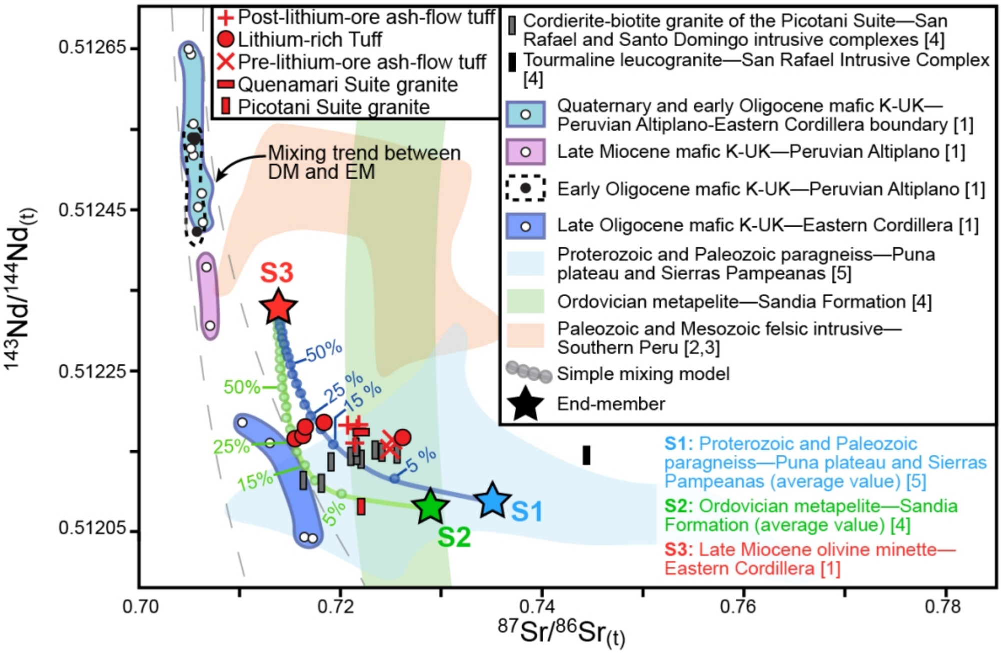

Fig. 10 Strontium and Nd isotope ratios corrected to 8.9 Ma of volcanogenic and intrusive rocks from the Macusani Volcanic Field and the San Rafael Intrusive Complex and compositional fields of regional rocks discussed in the main text. The compositional field of Proterozoic and Paleozoic paragneiss from the Puna Plateau and Sierras Pampeanas encompasses 80% of the corresponding data presented in Figure 8, thereby effectively excluding outliers. The selected crustal rock end-members represent average isotopic values of Proterozoic and Paleozoic paragneiss in the Puna plateau and Sierras Pampeanas (S1; DIGIS Team, 2023) and Ordovician metapelite of the Sandia Formation (S2; Harlaux et al., 2021). The selected mantle-derived end-member is a late Miocene (7.51 ± 0.05 Ma; $^{40}Ar/^{39}Ar$ phlogopite date, error 2σ) olivine minette from the Eastern Cordillera (Carlier et al. 2005). The employed models assume complete chemical mixing of two end-members resulting in a homogeneous mixture (i.e. hybridization; Heinonen et al., 2021). Percentages represent the fraction of the mantle-derived end-member. References: [1] Carlier et al. (2005); [2] Reitsma (2012); [3] Martínez et al. (2019); [4] Harlaux et al. (2021); [5] DIGIS Team (2023). Abbreviations: DM—Depleted mantle; EM—Enriched mantle.

112x73mm (300 x 300 DPI)

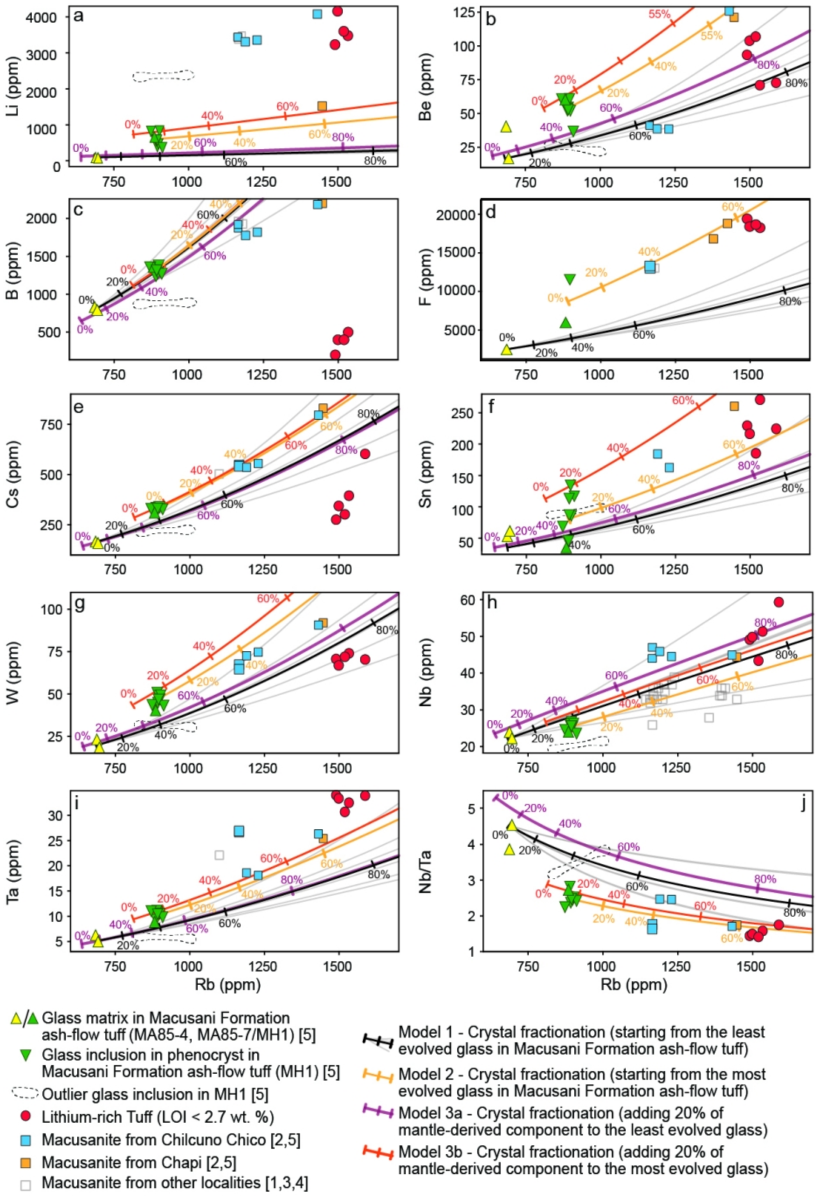

Fig. 11 Bivariant plots of Rb vs. elements that behaved as incompatible in parental magmas to Macusani Formation rocks including (a) Li, (b) Be, (c) B, (d) F, (e) Cs, (f) Sn, (g) W, (h) Nb, and (i) Ta, and (j) Nb/Ta ratio. Fractional crystallization is modeled as outlined in Rollinson & Pease (2021). The percentages indicate the proportion of crystal fractionation. Experimental mineral/melt partition coefficients in felsic peraluminous magmas of Villaros & Pichavant (2019) and Pichavant et al. (2024a) were employed. Thick lines represent models with a fractionated assemblage corresponding to average modal proportions of phenocrysts in ash-flow tuff as estimated by Pichavant et al. (1988a) [quartz (0.330), alkali feldspar (0.367), plagioclase (0.239), biotite (0.051), andalusite (0.007), and muscovite (0.006)]. Thin gray lines represent the six different phenocryst modes considered by Pichavant et al. (2024a) to account for the effect of antecryst recycling in long-lived, large-volume silicic systems. Curves with different colors represent melt evolution during crystallization-differentiation when initial melts are established as the least evolved glass in Macusani Formation ash-flow tuff (black line; Model 1) or the average of glass in the most evolved Macusani Formation ash-flow tuff (pale orange line; Model 2). The compositions of starting melts with an additional 20% mantle-derived contribution (Model 3; see calculation in Figs. S5 and S6) are also considered for the

aforementioned least (Model 3a; purple line) and most (Model 3b; dark orange line) evolved glasses. Given the little variation in the final products of hybridization with a mantle-derived component for the different considered degrees of fractional crystallization, a 30 % of crystallization was chosen as it represents and intermediate, plausible value. All Lithium-rich Tuff samples with LOI > 2.7 wt % or plotting outside the Rb-Sr isochrone were not considered in the plots. References: [1] Barnes et al. (1970); [2] Pichavant et al. (1987); [3] Pichavant et al. (1988b); [4] Craig et al. (2010); [5] Pichavant et al. (2024a).

206x303mm (150 x 150 DPI)

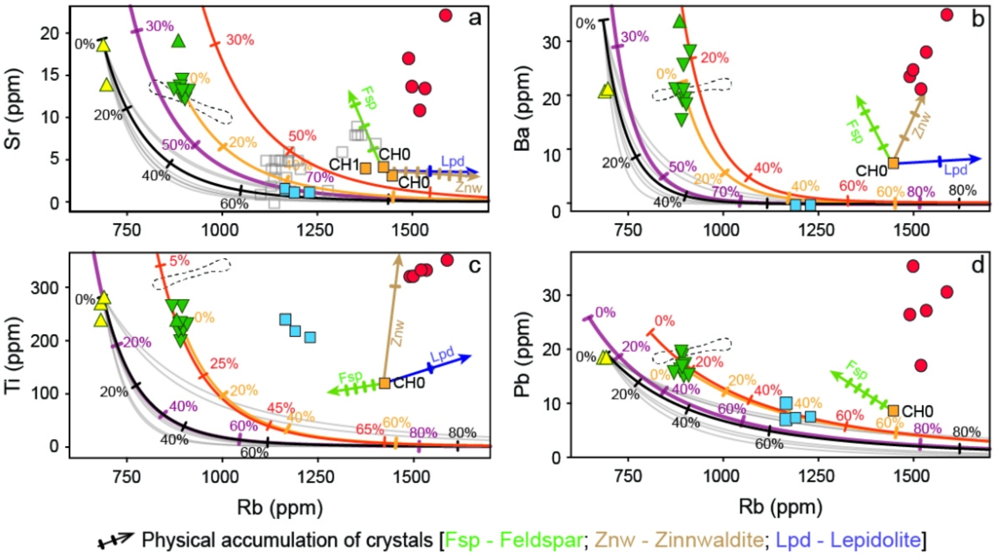

Fig. 12 Bivariant plots of Rb vs. elements that behaved as compatible in parental magmas to Macusani Formation rocks including (a) Sr, (b) Ba, (c) Ti, and (d) Pb. Fractional crystallization (curves) models were calculated using the same parameters and references as in Figure 11. Physical segregation (accumulation; arrows) of crystals was calculated by adding zinnwaldite, lepidolite, and feldspars at increasing 2% proportions to a glass with the average composition of the most evolved macusanite specimens (JV3, CH1, and CH0). The composition of Li-F micas was extracted from Torró et al. (2023) and the composition of feldspars was extracted from the most evolved feldspars in Macusani Formation ash-flow tuff as reported by Pichavant et al. (2024a).

198x111mm (150 x 150 DPI)

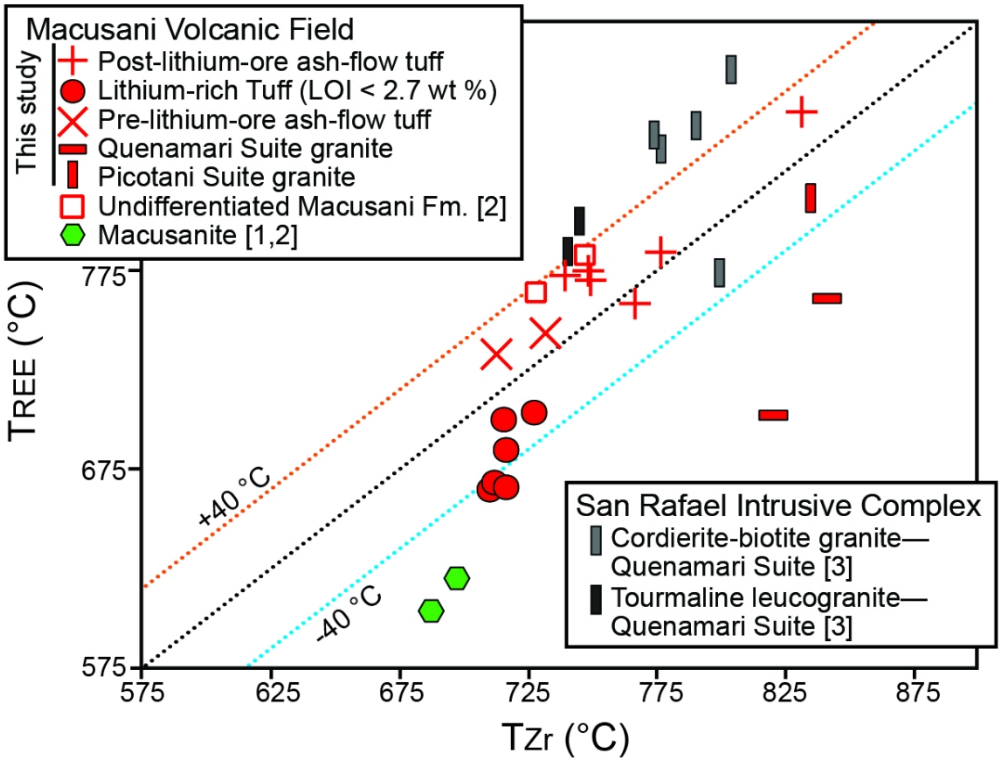

Fig. 13 T_{REE} (Montel, 1993) vs. T_{Zr} (Watson & Harrison, 1983) plot for volcanogenic and intrusive units in the Macusani Volcanic Field and intrusive rocks in the San Rafael intrusive complex. References: [1] Pichavant et al. (1987); [2] Pichavant et al. (1988b); [3] Harlaux et al. (2021).

103x78mm (300 x 300 DPI)

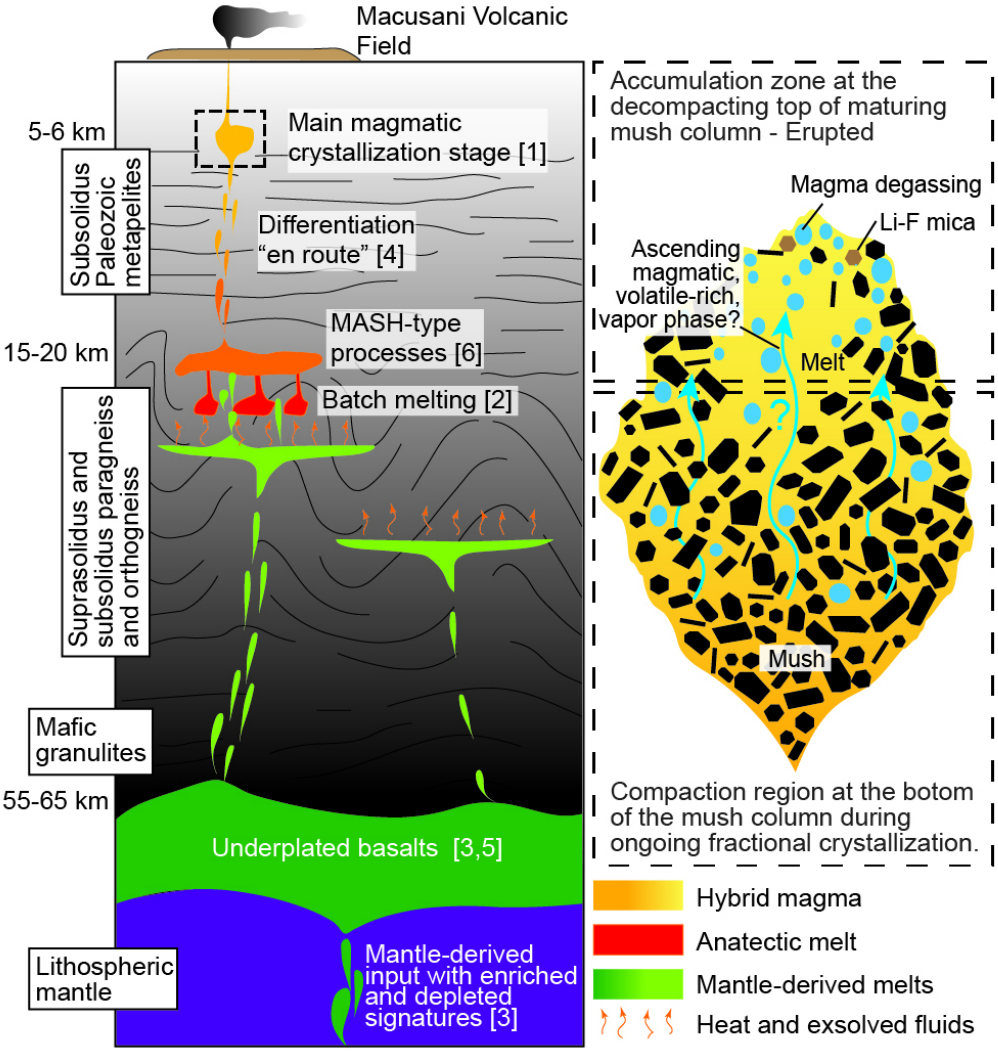

Fig. 14 Transcrustal magmatic model in the Eastern Cordillera of southern Peru for the genesis of magmas parental to Li-ore units in the Falchani Lithium Project. Mantle-derived input and different crustal magmatic reservoirs beneath the Macusani Volcanic Field are inspired in Pichavant et al. (1988b, 2024b). Lithospheric mantle, underplated basalts, and mafic granulites in accordance to the high wave speed anomaly reported by Garzione et al. (2017) and petrological interpretations of Carlier et al. (2005). The ~55-65 km crustal thickness during the late Miocene is based on Garzione et al. (2017). This overthickened crust is likely the result of crustal-scale thrust stacking (Perez et al., 2016; Baby et al., 2018). Fractional crystallization drove volatile exsolution and, potentially, fluid migration through the crystal mush, concentrating incompatible lithophile elements at the magma chamber roof. Pre-eruptive crystallization of Li-F micas retained lithium in the system, while their subsequent entrainment in the erupted products led to the high Li contents in the Falchani deposit. References: [1] Pichavant et al. (1988a); [2] Pichavant et al. (1988b); [3] Carlier et al. (2005); [4] Tartèse & Boulvais (2010); [5] Garzione et al. (2017); [6] Pichavant et al. (2024a).

82x86mm (300 x 300 DPI)

Table 1 Whole-rock radiogenic Sr, Nd, and Pb isotope results.

Sample	2021-MAC-003	2021-MAC-012	2021-MAC-025	2021-MAC-031
Lithotype	Quenamari Suite granite	Post-lithium-ore ash-flow tuff	Lithium-rich Tuff	Lithium-rich Tuff
Rb/Sr*	5.939871	2.437626	62.662358	144.106453
^{87}Rb/^{86}Sr	17.222766	7.066090	181.942717	419.170906
^{87}Sr/^{86}Sr	0.724218	0.721533	0.738421	0.756846
2σ	0.000005	0.000004	0.000005	0.000007
^{87}Sr/^{86}Sr$_{(t)}$	0.722041	0.720640	0.715426	0.703868
Sm/Nd*	0.256471	0.219041	0.257369	0.289327
^{147}Sm/^{144}Nd	0.158230	0.135137	0.158784	0.178500
^{143}Nd/^{144}Nd	0.512181	0.512190	0.512176	0.513000
2σ	0.000007	0.000007	0.000005	0.000006
^{143}Nd/^{144}Nd$_{(t)}$	0.512172	0.512182	0.512167	0.512990
εNd$_{(t)}$	-8.5	-8.3	-8.6	7.4
Sm/Nd T$_{DM}$	2.33	1.62	2.37	0.21
U/Pb*	0.3425	0.1324	0.4183	0.7504
Th/U*	0.3983	1.5775	0.2122	0.1884
^{206}Pb/^{204}Pb	18.8691	18.8289	18.9329	18.9753
1σ	0.0009	0.0033	0.0008	0.0008
^{207}Pb/^{204}Pb	15.6943	15.6874	15.6926	15.7041
1σ	0.0007	0.0027	0.0007	0.0007
^{208}Pb/^{204}Pb	38.9525	38.9628	38.8560	38.9346
1σ	0.0019	0.0067	0.0017	0.0017
^{206}Pb/^{204}Pb$_{(t)}$	18.8404	18.8178	18.8978	18.9123
^{207}Pb/^{204}Pb$_{(t)}$	15.6930	15.6869	15.6910	15.7011
^{208}Pb/^{204}Pb$_{(t)}$	38.9524	38.9621	38.8559	38.9345

Isotopic ratios were corrected for an age of 8.9 Ma based on ^{40}Ar/^{39}Ar dates on mica crystals fr

We used the following decay constants (λ) for calculations: λ(^{87}Rb) = 1.42 x 10^{-11} years^{-1} (Steig

Chondrite Uniform Reservoir (CHUR) values are used to calculate the εNd$_{(t)}$ values [εNd$_{(t)}$=((

Sm/Nd T$_{DM}$ ages are calculated using the depleted mantle model of DePaolo (1981).

*Measured by ICP-MS (this study).

2021-MAC-033 Post-lithium-ore ash-flow tuff	2021-MAC-034 Post-lithium-ore ash-flow tuff	2021-MAC-038 Lithium-rich Tuff	2021-MAC-039 Lithium-rich Tuff	2021-MAC-040 Lithium-rich Tuff
2.636161	2.554153	123.684365	140.065148	109.655500
7.642233	7.404578	360.285536	407.854388	318.949068
0.722388	0.722510	0.771622	0.767905	0.756449
0.000006	0.000005	0.000006	0.000006	0.000005
0.721422	0.721574	0.726086	0.716357	0.716138
0.228766	0.218259	0.199712	0.245339	0.248148
0.141137	0.134655	0.123212	0.151362	0.153095
0.512168	0.512190	0.512174	0.512189	0.512178
0.000006	0.000005	0.000007	0.000008	0.000007
0.512160	0.512182	0.512167	0.512180	0.512169
-8.8	-8.3	-8.6	-8.4	-8.6
1.80	1.61	1.43	2.04	2.13
0.0691	0.1251	0.3768	0.6467	0.6854
0.7793	0.6810	0.1709	0.2634	0.1253
18.8448	18.8395	18.9160	18.9155	18.9767
0.0011	0.0008	0.0003	0.0002	0.0013
15.6903	15.6920	15.6921	15.6923	15.6864
0.0009	0.0007	0.0003	0.0002	0.0011
38.9725	38.9756	38.9256	38.9298	38.9029
0.0023	0.0017	0.0007	0.0006	0.0026
18.8448	18.8395	18.8844	18.8612	18.9191
15.6900	15.6915	15.6906	15.6898	15.6838
38.9721	38.9753	38.9255	38.9297	38.9029

om the Lithium-rich Tuff (unpublished data). All calculations are done following the procedure

ger & Jager, 1977), $\lambda(^{147}Sm) = 6.54 \times 10^{-12}$ years^{-1} (Lugmair & Marti, 1978), $\lambda(^{238}U) = 0.01551$

$^{43}Nd/^{144}Nd_{(rock,t)}/^{143}Nd/^{144}Nd_{(CHUR,t)})-1)x10^{4}]$ (Rollinson & Pease, 2021). The present-day $^{143}Nd/$

2021-MAC-045 Pre-lithium-ore ash-flow tuff	2021-MAC-046 Pre-lithium-ore ash-flow tuff	2021-MAC-047 Post-lithium-ore ash-flow tuff	2021-MAC-048 Lithium-rich Tuff	2021-MAC-055 Picotani Suite granite
6.405349	6.056142	2.719262	87.639075	2.106763
18.577863	17.564721	7.883145	254.762456	6.107737
0.727213	0.727031	0.722391	0.750461	0.722775
0.000004	0.000004	0.000005	0.000006	0.000005
0.724865	0.724811	0.721395	0.718262	0.722003
0.204957	0.211923	0.213494	0.287275	0.266563
0.126448	0.130746	0.131715	0.177234	0.164456
0.512172	0.512160	0.512185	0.512196	0.512090
0.000007	0.000006	0.000003	0.000006	0.000008
0.512165	0.512152	0.512177	0.512186	0.512080
-8.7	-8.9	-8.4	-8.2	-10.3
1.49	1.59	1.56	3.67	2.95
0.2156	0.1504	0.2586	0.6026	0.2204
0.4150	0.4032	0.6592	0.2046	2.1871
18.8622	18.8365	18.8571	18.9666	18.8046
0.0005	0.0005	0.0005	0.0003	0.0004
15.6927	15.6909	15.6914	15.6931	15.6901
0.0004	0.0004	0.0005	0.0003	0.0003
38.9467	38.9423	38.9691	38.9280	38.9720
0.0010	0.0011	0.0011	0.0007	0.0009
18.8622	18.8365	18.8571	18.9160	18.7861
15.6919	15.6903	15.6904	15.6907	15.6893
38.9465	38.9421	38.9688	38.9279	38.9710

described in Faure & Mensing (2005).

25 x 10^{-9} years^{-1}, λ(^{235}U) = 0.98485 x 10^{-9} years^{-1}, and λ(^{232}Th) = 0.049475 x 10^{-9} years^{-1} (Steig

/^{144}Nd$_{CHUR}$ ratio normalized against ^{146}Nd/^{144}Nd = 0.7219 is extracted from Goldstein et al. (198 ger & Jager, 1977).

34). The $^{143}Nd/^{144}Nd_{CHUR}$ ratio at a time t is calculated considering a Sm/Nd_{CHUR} ratio of 0.325 (W

Vasserburg et al., 1981).